Simulated Milky Way analogues: implications for dark matter direct searches

Nassim Bozorgnia,[a] **Francesca Calore,**[a] **Matthieu Schaller,**[b] **Mark Lovell,**[a,c] **Gianfranco Bertone,**[a] **Carlos S. Frenk,**[b] **Robert A. Crain,**[d] **Julio F. Navarro,**[e,f] **Joop Schaye**[g] **and Tom Theuns**[b]

[a]GRAPPA, University of Amsterdam,
 Science Park 904, 1090 GL Amsterdam, Netherlands
[b]Institute for Computational Cosmology,
 Durham University, South Road, Durham DH1 3LE, UK
[c]Instituut-Lorentz for Theoretical Physics,
 Niels Bohrweg 2, NL-2333 CA Leiden, Netherlands
[d]Astrophysics Research Institute, Liverpool John Moores University,
 146 Brownlow Hill, Liverpool L3 5RF, UK
[e]Department of Physics & Astronomy, University of Victoria,
 Victoria, BC, V8P 5C2, Canada
[f]Senior CIfAR Fellow
[g]Leiden Observatory, Leiden University,
 PO Box 9513, NL-2300 RA Leiden, Netherlands

 E-mail: n.bozorgnia@uva.nl

Abstract. We study the implications of galaxy formation on dark matter direct detection using high resolution hydrodynamic simulations of Milky Way-like galaxies simulated within the EAGLE and APOSTLE projects. We identify Milky Way analogues that satisfy observational constraints on the Milky Way rotation curve and total stellar mass. We then extract the dark matter density and velocity distribution in the Solar neighbourhood for this set of Milky Way analogues, and use them to analyse the results of current direct detection experiments. For most Milky Way analogues, the event rates in direct detection experiments obtained from the best fit Maxwellian distribution (with peak speed of $223 - 289$ km/s) are similar to those obtained directly from the simulations. As a consequence, the allowed regions and exclusion limits set by direct detection experiments in the dark matter mass and spin-independent cross section plane shift by a few GeV compared to the Standard Halo Model, at low dark matter masses. For each dark matter mass, the halo-to-halo variation of the local dark matter density results in an overall shift of the allowed regions and exclusion limits for the cross section. However, the compatibility of the possible hints for a dark matter signal from DAMA and CDMS-Si and null results from LUX and SuperCDMS is not improved.

Keywords: dark matter theory, dark matter experiments, dark matter simulations

Contents

1 Introduction

Dark matter (DM) direct detection searches aim to measure the recoil energy of a nucleus in a low background detector induced by the scattering of Weakly Interacting Massive Particles (WIMPs), one of the most well-motivated classes of particle DM candidates, from the dark halo of the Milky Way (MW). In the last few years, a number of direct detection experiments have reported hints for signals that could be interpreted as signatures of DM interactions. Currently, only hints from the DAMA/LIBRA [1] and CDMS-II [2] experiments remain. These hints, however, are in tension with the null results from many other experiments, including LUX (Large Underground Xenon) [3] and SuperCDMS [4], which set the strongest exclusion limits in the spin-independent DM–nucleon cross section and WIMP mass plane at large (> 6 GeV) and small (3.5–6 GeV) WIMP masses, respectively.

There are large systematic uncertainties in the interpretation of the data from DM direct detection experiments due to the uncertainties in the DM density and velocity distribution at the position of the Sun. Indeed, in order to show the preferred regions and exclusion limits in the DM mass and scattering cross section plane, one needs to make assumptions about

the DM halo properties, namely the local DM density and DM velocity distribution. The simplest and most commonly adopted DM halo model is the Standard Halo Model (SHM): it assumes an isothermal, spherical DM halo with an isotropic Maxwell-Botzmann DM velocity distribution. In this model, the local DM density is usually assumed to be 0.3 GeV/cm^3; the local velocity distribution in the Galactic rest frame is assumed to be a Maxwellian with a most probable (peak) speed equal to the local circular speed v_c (usually assumed to be 220 km/s), a three-dimensional velocity dispersion of $\sqrt{3/2}\,v_c$, and truncated at the escape speed of 544 km/s from the Galaxy. Throughout this paper, when referring to the SHM Maxwellian, we consider the Maxwellian distribution with a most probable speed of 230 km/s in order to be consistent with the local circular speed assumed in deriving the observed MW rotation curves [5] (see section 3 for more details).

The local DM density enters as a normalisation factor in the event rate in direct detection experiments, whilst the DM velocity distribution enters in the event rate in a more complicated way (see eq. (6.1)). In particular, different direct detection experiments with different energy thresholds and target nuclei probe different DM speed ranges, and thus their dependence on the DM velocity distribution varies. To overcome the astrophysical uncertainties in the interpretation of direct detection results, methods to compare the results of different experiments in a halo-independent way have been developed and applied to direct detection data [6–25]. Such methods are based on comparing different experiments in the space of the minimum DM speed, $v_{\min}$, required for a DM particle to deposit a recoil energy E_R in the detector, and thus can only be applied to compare experiments which are sensitive to the same range of $v_{\min}$.

High resolution numerical simulations of galaxy formation can provide information on the properties of the DM halo. Velocity distributions extracted from high resolution DM-only (DMO) simulations deviate substantially from a Maxwellian distribution, with fewer particles at the peak and an excess of particles at large speeds [26, 27]. DMO simulations can achieve high resolution, but have significant systematic uncertainties since they neglect the effect of the baryonic components during the galaxy formation process. Additionally, velocity distributions drawn from isolated simulations of the MW and the accretion of the Sagittarius dwarf galaxy show significant deviations from the best fit Maxwellian distribution, and this has important effects on direct detection rates [28]. Nevertheless, the local DM distribution is expected to be very smooth: high resolution N-body simulations predict that the density at the Solar radius can differ from the mean over the best-fit ellipsoidal equidensity contour by at most 15% at the 99.9% confidence level [26].

Recently, realistic cosmological simulations including baryons have become possible thanks to advances in physical modeling, as well as better understanding and treatment of numerical issues. The hydrodynamic simulation performed by Ling *et al.* [29] predicts a DM speed distribution which deviates significantly from the Maxwellian, and instead gives an excellent fit to a Tsallis [30] distribution[1]. In this simulation, the local DM density is found to be 0.37 – 0.39 GeV/cm^3. The Eris hydrodynamic simulation [32] finds a speed distribution that is not a perfect Maxwellian, with an excess of particles at speeds less than 350 km/s compared to the SHM Maxwellian and fewer particles at higher speeds. The speed distribution is instead well fit by the fitting function proposed by Mao *et al.* [33]. The NI-

---

[1]See also ref. [31] for a variation of the Tsallis distribution function which is anisotropic.

HAO (Numerical Investigation of a Hundred Astrophysical Objects) simulations [34] find a DM speed distribution which is very different from the Maxwellian, being more symmetric around the peak velocity and falling rapidly at large velocities, thus agreeing with the results of the Eris simulation. All these hydrodynamic simulations help build an understanding of the processes that can shape and modify the local DM density and velocity distribution. However, to make more precise quantitative predictions it is necessary that all these effects are modeled in such a way that the main galaxy population properties are broadly reproduced. This ensures, for instance, that appropriate amounts of feedback are applied and that the corresponding impact of feedback on DM is reasonably realistic.

In this work, we study the implications of simulated MW-like galaxies within the EAGLE ("Evolution and Assembly of GaLaxies and their Environments") [35, 36] and APOSTLE [37, 38] projects for DM direct detection. The EAGLE project is a suite of hydrodynamic simulations that are calibrated to reproduce the observed distribution of stellar masses and sizes of low-redshift galaxies as well as the relation between the stellar mass and black hole mass of galaxies; in this respect they are unique amongst simulations of galaxy formation. In a companion paper, we have studied the implications of the EAGLE and the related APOSTLE simulations for DM indirect detection [39]. We first consider a selection of MW-like galaxies within haloes with virial mass in the range $\mathcal{O}(10^{12} - 10^{13})\,\mathrm{M}_\odot$. We then impose a set of selection criteria crucial for accurately predicting the local DM density and velocity distribution. Namely, we require that the haloes satisfy observational constraints on the MW rotation curve [5], and have stellar masses within the observed MW stellar mass range. We then extract the local DM density and velocity distribution for the selected haloes, and use them to analyse current data from direct detection experiments.

The paper is outlined as follows. In section 2 we present the set of EAGLE and APOSTLE cosmological hydrodynamic simulations used in this work. In section 3 we discuss in detail the selection criteria used for choosing MW analogues, and how each criterion is relevant for determining the local DM distribution. In sections 4 and 5 we present the local DM velocity distribution and DM density extracted from the simulations. In section 6 we introduce the formalism for computing the predicted signals in DM direct detection experiments. In section 7 we perform an analysis of current direct detection data and discuss how the allowed regions and exclusion limits set by different experiments in the DM mass and scattering cross section plane changes when the DM distribution of simulated haloes is used. Finally, in section 8 we summarize the conclusions of this work. In Appendices A, B, and C, we provide additional material relevant for this work.

2 Simulations

The simulations used in this study comprise parts of the EAGLE [35, 36] and APOSTLE [37, 38] projects, both of which we describe below.

The EAGLE project combines a state-of-the-art hydrodynamical SPH implementation nicknamed ANARCHY [40, 41] – built on top of an optimized version of the GADGET SPH code, last described by [42] – and a detailed subgrid model of galaxy formation that features metal-line cooling, photo-reionization, star formation, and feedback from star formation and active galactic nuclei [43–47]. The subgrid model is regulated by a number of parameters, which are calibrated to give a good fit to the $z = 0.1$ galaxy stellar mass function and to the

observed relation between galaxy stellar mass and size for disc galaxies. From the suite of EAGLE simulations we select candidate MW analogues in the high resolution $(25 \text{ Mpc})^3$ box (initial gas particle mass $2.26 \times 10^5 \text{ M}_\odot$), which adopts the Planck cosmological parameters [48] ($\Omega_m = 0.307$, $\Omega_\Lambda = 0.693$, $\Omega_b = 0.0482$, $h = 0.678$, $\sigma_8 = 0.83$, and $n_s = 0.961$) and the EAGLE model parameters re-calibrated for high resolution (see ref. [35] for a discussion of model parameter calibration). Throughout the paper, we refer to this simulation as EAGLE HR. Notice that in other EAGLE papers, this simulation is referred to as Recal-L025N0752.

As we will discuss in section 3, the initial set of EAGLE HR haloes with the virial mass in the range $\mathcal{O}(10^{12} - 10^{13}) \text{ M}_\odot$ consists of 61 objects. To increase our initial number of haloes, we also consider haloes within the APOSTLE project. The APOSTLE project applies the EAGLE model in a series of zoomed simulations of Local Group-analogue systems. Each Local Group volume contains two haloes of mass $\sim 10^{12} \text{ M}_\odot$, each of which hosts a potential MW galaxy analogue. We picked our candidate galaxies from the 12 intermediate resolution, comparable in resolution to EAGLE HR, volumes as presented in ref. [37]. We refer to these simulations collectively as APOSTLE IR. These simulations were run with the same code as EAGLE, used the EAGLE reference parameters as calibrated for the EAGLE intermediate resolution simulations, and were run with the WMAP7 cosmological parameters ($\Omega_m = 0.272$, $\Omega_\Lambda = 0.728$, $\Omega_b = 0.0455$, $h = 0.704$, $\sigma_8 = 0.81$, and $n_s = 0.967$); the initial gas particle mass is $1.2 \times 10^5 \text{ M}_\odot$.

For both EAGLE HR and APOSTLE IR, companion simulations were run with all of the matter content treated as collisionless, and in this work we compare the results of these DMO runs with those that use the full hydrodynamical treatment.

Notice that we have not performed resolution tests for the simulations used in this work. Lower resolution simulations compared to EAGLE HR and APOSTLE IR cannot be used to test for numerical convergence because there would be insufficient particles to probe the DM distribution in the Solar neighbourhood. Re-calibrated higher resolution simulations are not available either. The caveat is that without such a test, it remains to be demonstrated that the conclusions of this work are robust with respect to the numerical resolution.

3   Selection of Milky Way-like galaxies

In ref. [39] we identified simulated galaxies that are "good" MW analogues according to the following three criteria: (i) their rotation curves provide good fits to the recent compilation of observed MW rotation curve from ref. [5], (ii) their stellar masses are within the 3σ observed stellar mass range of the MW, $4.5 \times 10^{10} < M_*/\text{M}_\odot < 8.3 \times 10^{10}$ [49], and (iii) they contain a substantial stellar disc component. The details of our selection procedure are presented in ref. [39]. Note that in deriving the measured MW rotation curves from ref. [5], we assume as fiducial values a local circular speed of $v_c = 230$ km/s, a local galactocentric distance of $R_0 = 8$ kpc, and the component of the Solar peculiar velocity in the direction of the Galactic rotation of $V_\odot = 12.24$ km/s [50].

We first consider all central galaxies in haloes with $5 \times 10^{11} < M_{200}/\text{M}_\odot < 2 \times 10^{13}$, where M_{200} is the mass enclosed within the sphere centered on the galaxy's potential minimum, that contains a mean density 200 times the critical density. These initial sets of galaxies comprise 61 and 24 objects for the EAGLE HR and APOSTLE IR simulations respectively, and
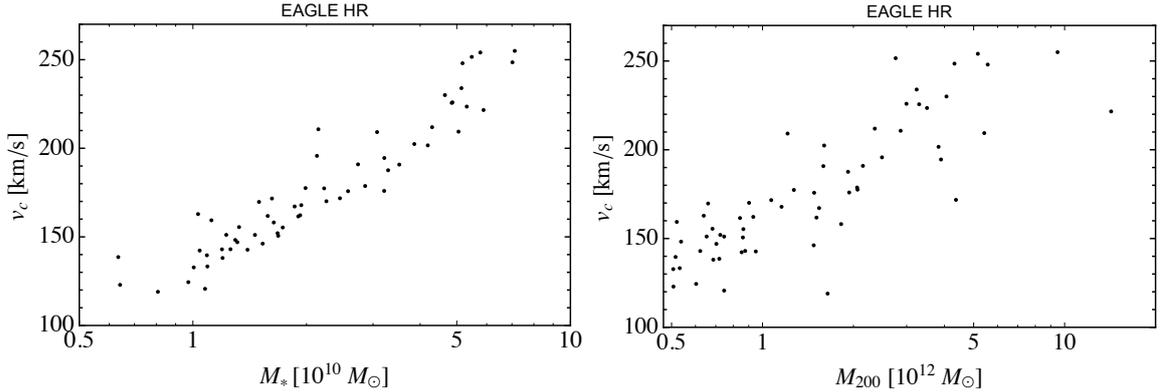
Figure 1. The correlation of the local circular speed at $R_0 = 8$ kpc with the total stellar mass, M_* (left panel) and the virial mass, M_{200} (right panel) for all the haloes with $5 \times 10^{11} < M_{200}/M_\odot \leq 1.4 \times 10^{13}$ in the EAGLE HR simulation.

the largest M_{200} in these sets is $1.4 \times 10^{13} M_\odot$. The final sets of galaxies that satisfy the three mentioned selection criteria consist of 2 objects for each project at our chose resolution.

Given the limited statistics once the selection criteria have been applied, we discuss below how each selection criterion affects the implications for direct detection, in particular the two main astrophysical inputs for computing direct detection rates, and examine whether it is possible to relax one or more of the criteria.

The local DM density and velocity distribution of the simulated haloes are important parameters for direct DM detection. Among the three initial criteria for identifying MW analogues, criteria (i) and (ii) are important because they directly affect the local circular speed, v_c, at the Solar radius, and hence the peak of the local DM speed distribution in the Galactic reference frame. In particular, the fit to the observed MW rotation curve constrains v_c. Also, as can be seen from figure 1, the stellar mass, M_*, is strongly correlated with v_c at 8 kpc, while the correlation of M_{200} with v_c is weaker. The Pearson's correlation coefficient between v_c and M_* is 0.94, while it is 0.68 between v_c and M_{200}.

The reason is that v_c at the Solar circle depends on the total mass in stars, gas and DM enclosed within the sphere of radius 8 kpc. The enclosed stellar mass within the Solar circle is a large fraction of the total stellar mass, $(0.5 - 0.9)M_*$ depending on the simulated halo in the EAGLE HR and APOSTLE IR run, since the enclosed stellar mass does not increase significantly with galactocentric distance beyond the Solar circle. On the other hand, the enclosed DM mass increases significantly with galactocentric distance, and the total mass enclosed within 8 kpc is only $(0.01 - 0.1)M_{200}$. Over the small halo mass range probed, we find little correlation between the DM mass enclosed within a sphere of radius 8 kpc and M_{200}. The scatter in galaxy stellar mass at a fixed halo mass dominates the variation in v_c. A stronger correlation between v_c and M_* compared to the correlation with M_{200} is hence found.

On the other hand, having a substantial stellar disc component, as specified by criterion (iii), for the simulated galaxies does not have an important effect on the local DM density and speed distributions. In particular, haloes which satisfy criteria (i) and (ii) but are spheroidal have DM velocity distributions similar to those with a disc. The local DM density range for

Halo Name	$M_*[\times 10^{10}\,\mathrm{M_\odot}]$	$M_{200}[\times 10^{12}\,\mathrm{M_\odot}]$	D/T	$\chi^2/(N-1)$
E1	5.88	14.26	0.18	105.54
E2	7.12	9.48	0.33	324.31
E3	5.77	5.16	0.35	190.97
E4	5.14	3.24	0.18	44.70
E5	5.18	5.57	0.14	160.27
E6	5.05	5.42	0.10	266.83
E7	7.02	4.32	0.25	160.58
E8	4.65	4.06	0.13	55.07
E9	5.31	3.50	0.45	74.55
E10	4.85	3.30	0.36	59.65
E11	5.48	2.76	0.46	220.96
E12	4.87	2.99	0.25	45.45
A1	4.88	1.64	0.70	221.27
A2	4.48	2.15	0.50	51.04

Table 1. Total stellar mass, halo mass, disc-to-total mass ratio D/T (defined in eq. (3.4) of ref. [39]), and reduced χ^2 for the fit to the rotation curve data (for $R > 2.5$ kpc) of the MW-like galaxies that satisfy our selection criteria (i) and (ii) in the EAGLE HR (haloes E1 to E12) and APOSTLE IR (haloes A1 and A2) runs.

all haloes satisfying criteria (i) and (ii) is slightly increased compared to the range for haloes satisfying all three criteria (see appendix A). This is due to the addition of more haloes to our sample, but without a significant trend in a specific direction. Thus, we believe that the predictions for direct detection searches remain unchanged for galaxies that do not have a substantial disc component.

Analogously to ref. [39], we define a second set of MW-like galaxies for each project at our chosen resolution, which satisfy only criteria (i) and (ii). This set consists of 12 galaxies in the EAGLE HR, and 2 galaxies in the APOSTLE IR simulations. Note that only 2 galaxies in the APOSTLE IR run have a stellar mass compatible with the observed range of MW stellar mass, and both of these galaxies also have a dominant stellar disc component. Therefore, it is not possible to increase the number of MW analogues in the APOSTLE IR run by relaxing the criterion on the stellar disc. In table 1 we list the parameters of the MW-like galaxies satisfying criteria (i) and (ii). In the main sections of this paper we only consider the set of galaxies which satisfy these two criteria. For completeness and comparison, we list the results for the two galaxies in the EAGLE HR simulation (E9 and E11 in table 1) which satisfy all three criteria in Appendix A.

In computing the goodness of fit to the observed MW rotation curves from ref. [5], we have considered measurements for galactocentric distances $R > 2.5$ kpc, since at smaller radii the gravitational potential of the Galactic bulge can break the assumption of circular orbits for the tracers in ref. [5]. The reduced χ^2 for the fit to the rotation curve data is in the range 44.70 – 324.31 (51.04 –221.27), for the EAGLE HR (APOSTLE IR) simulation. Since we are interested in the local DM distribution, we would like to check how the goodness of fit changes if a smaller range of R is considered. In particular, we consider four additional ranges of R for the fit: $R > 5$ kpc, $R > 7$ kpc, 5 kpc $< R <$ 11 kpc, and 7 kpc $< R <$ 9 kpc.

For all these cases, the goodness of fit is only marginally better for most haloes with M_* within the observed MW stellar mass range in the EAGLE HR and APOSTLE IR simulations, and the overall range of the reduced χ^2 is slightly smaller. For the EAGLE HR (APOSTLE IR) simulation, the reduced χ^2 range is 22.28 – 290.36 (44.6 –213.24), 17.20 – 182.91 (41.40 –134.16), 24.29 – 317.92 (48.92 – 233.42), and 23.71 – 268.92 (59.86 – 196.92) when taking measurements at $R > 5$ kpc, $R > 7$ kpc, 5 kpc $< R <$ 11 kpc, and 7 kpc $< R <$ 9 kpc, respectively. The reason for this small reduction in the reduced χ^2 values is that the measured MW rotation curves have very small error bars at small galactocentric distances, $R < 5$ kpc, and therefore the fit gets worse when including the measurements at 2.5 kpc $< R < 5$ kpc.

As discussed in ref. [39], the halo masses of our selected simulated galaxies are higher than the MW halo mass expected from abundance matching arguments (e.g. $M_{200,\mathrm{MW}} = 1.2^{+0.7}_{-0.4} \times 10^{12}\,\mathrm{M}_\odot$ [51]) probably due to the slightly too efficient feedback in the EAGLE HR simulated haloes of this mass range [35, 36]. We have checked that the large halo masses and the mismatch between stellar mass and halo mass do not affect the recoil rate and other relevant quantities in direct DM detection experiments. Note that the higher halo mass results in a higher DM escape speed from the Galaxy, and hence a higher velocity tail of the DM velocity distribution. However, the halo integral (see section 6.2), which encodes the astrophysical dependence of the recoil rate, is very similar for haloes which have the highest and smallest halo masses but with stellar masses within the 3σ observed MW stellar mass range.

4   Dark matter velocity distribution

The event rates in a direct detection experiment depend strongly on the DM velocity distribution at the position of the Sun. In this section we discuss the DM velocity distribution in the Galactic rest frame for the EAGLE HR and APOSTLE IR simulated haloes which satisfy criteria (i) and (ii) as defined in section 3.

To find the DM velocity distribution at the Solar circle ($R_0 = 8$ kpc), we consider a torus with a square cross section which is aligned with the stellar disk, and has an inner and outer radius of 7 kpc and 9 kpc from the Galactic centre respectively, and a height extending from -1 kpc to 1 kpc with respect the the Galactic plane. This region contains a total of 1821 – 3201 (2160 – 3024) particles depending on the halo in the EAGLE HR (APOSTLE IR) simulation. Notice that due to the limited resolution of the simulation, we are not sensitive to the local variation of the DM velocity distribution within the torus. Hence we take the average velocity distribution of DM particles in the full torus, instead of computing it at the azimuthal position of the Sun at 8 kpc in the torus.

We define a reference frame in the plane of the galaxy to describe the velocity vector of the simulation particles. In this reference system, the origin is at the Galactic centre, the z-axis is perpendicular to the stellar disk, r is in the radial direction, and θ is in the tangential direction. In the case of the DMO simulations, we orientate the torus in the same direction as in the hydrodynamic case. We can then calculate the velocity distribution for the vertical (v_z), radial (v_r), and azimuthal (v_θ) components of the DM in addition to the velocity modulus distribution. This distribution, as well as the three components of the velocity distribution, are individually normalised to unity, such that $\int dv f(|\mathbf{v}|) = 1$ and $\int dv_i f(v_i) = 1$ for $i = z, r, \theta$. Note that the velocity modulus distribution, $f(|\mathbf{v}|)$, normalised

in this way is related to the velocity distribution, $\tilde{f}(\mathbf{v})$, by,

$$f(|\mathbf{v}|) = v^2 \int d\Omega_{\mathbf{v}} \tilde{f}(\mathbf{v}), \tag{4.1}$$

such that $\int d^3 v \tilde{f}(\mathbf{v}) = 1$. Here $d\Omega_{\mathbf{v}}$ is an infinitesimal solid angle around the direction $\mathbf{v}$.

In sections 4.1 and 4.2 we present the velocity modulus distribution, as well as the components of the velocity distribution of the selected simulated haloes, and discuss how they can be described using fitting functions. Notice that in the analysis of direct detection data in section 7, we use the velocity distributions extracted directly from the simulations instead of the best fit functions.

4.1 Velocity modulus distribution

In the left panels of figure 2, we show the local DM velocity modulus distribution in the Galactic rest frame for two haloes in the EAGLE HR (top panel) and APOSTLE IR (bottom panel) simulations that satisfy our selection criteria. From the 12 MW-like EAGLE HR haloes, in the top panel we only show the velocity modulus distribution for the two haloes that have speed distributions closest to (halo E12; reduced χ^2 of 1.43) and farthest from (halo E3; reduced χ^2 of 23.4) the SHM Maxwellian distribution (with peak speed of 230 km/s). The vertical error bars specify the 1σ Poisson error on the data points, and the horizontal error bars specify the speed bin size. The Maxwellian speed distribution (with peak speed of 230 km/s) is shown as solid black lines, and the best fit Maxwellian speed distributions are also shown as dashed coloured curves.

One potential issue with the vertical error bars on the data points is that they might be correlated. Therefore, we have checked that bootstrap-resampling the distributions leads to similar error estimators compared to simple Poisson statistics. Hence, we will use the 1σ Poisson error on the data points for our analysis in the rest of the paper. Notice also that we have considered different speed bin sizes and found the optimal size to be 25 km/s. A smaller bin size would increase the noise in the data points due to the small number of particles in each bin, while a larger bin size would smear out features in the speed distribution.

In the right panels of figure 2 we show the velocity modulus distributions for the same haloes shown in the left panels but in the corresponding DMO simulations. Comparing the left and right panels of the figure, it is clear that baryons have an important effect on the DM speed distribution at the Solar radius. Including baryons in the simulation leads to a shift of the peak of the local DM speed distribution to higher speeds. This happens because baryons are dissipative and hence deepen the gravitational potential of the Galaxy in the inner regions, resulting in more high velocity particles, thus shifting the peak of the DM speed distribution to larger values.

For comparison, in Appendix B we show the velocity modulus distributions for our selected haloes in the EAGLE HR simulation that have the smallest (halo E6) and largest (halo E4) local DM density. It is clear from figure 14 that the speed distributions for the two haloes are similar, as expected, since the local DM density does not affect the DM speed distributions.

Note that the local Galactic escape speeds for some haloes in the EAGLE HR simulation are higher than the value of the MW escape speed at the Solar position found recently by the RAVE survey, $v_{\rm esc} = 533^{+54}_{-41}$ km/s [53]. Although the RAVE value of the escape speed
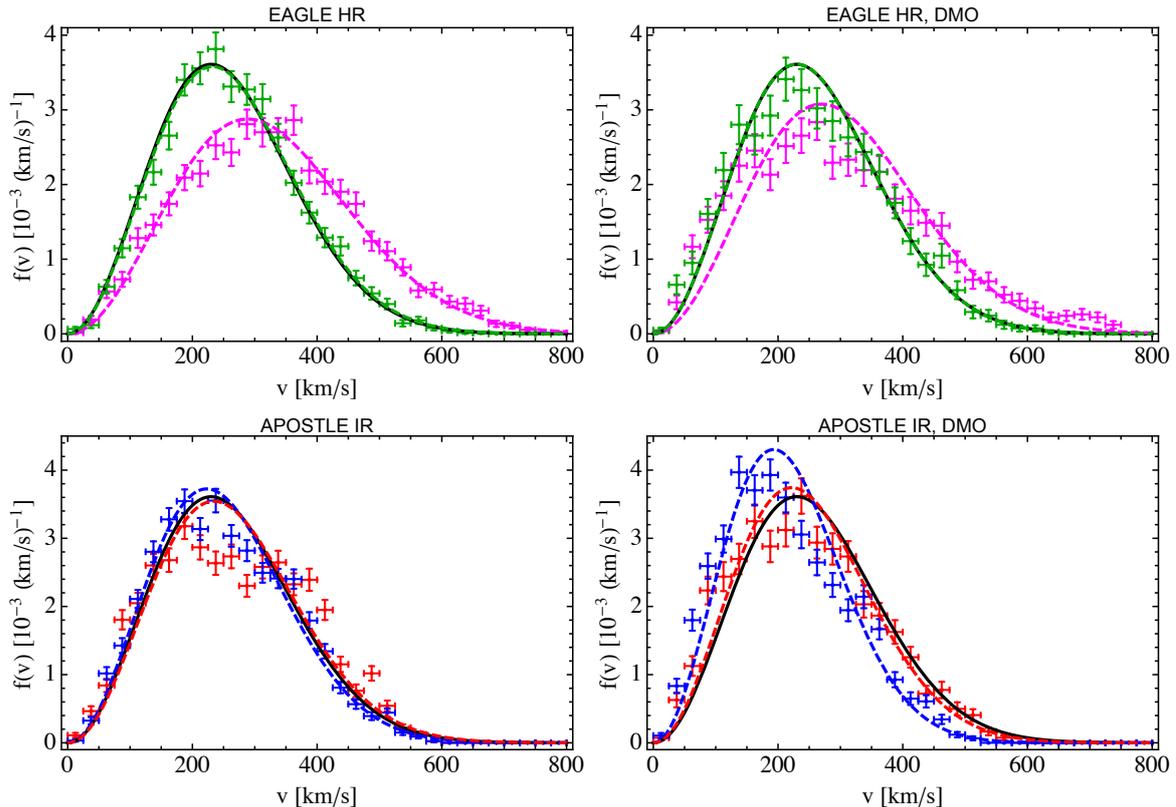
Figure 2. DM velocity modulus distributions in the Galactic rest frame (coloured data points with 1σ error bars) for two haloes in the EAGLE HR simulation which satisfy our selection criteria and have the speed distributions closest to (halo E12, shown in green) and farthest from (halo E3, shown in magenta) the SHM Maxwellian (top left), and two haloes in the APOSTLE IR simulation satisfying our selection criteria (bottom left). The right panels show the velocity modulus distributions for the same haloes shown in the left panels but in a DMO simulation. The black solid line shows the SHM Maxwellian speed distribution (with peak speed of 230 km/s), and the coloured dashed lines show the best fit Maxwellian distribution for each halo (with matching colours).

is actually a lower limit on the true MW escape speed, it is the commonly adopted value. Also, the larger $v_{\rm esc}$ values of the haloes in the EAGLE HR simulation are due to the larger M_{200} of those haloes compared to the MW. However, as discussed in section 3, this does not affect the predicted signals in direct detection experiments. The local Galactic escape speeds are in the range of 720 – 1083 km/s (617 – 646 km/s) for the selected EAGLE HR (APOSTLE IR) haloes. These escape speeds are computed for each simulated halo from the total mass enclosed in a sphere of radius 7 kpc, which is the inner radius of our defined torus. Therefore, these escape speeds represent an upper limit on those expected at the Solar circle.

We now discuss how well the DM velocity modulus distributions of the simulated MW analogues can be fitted with various fitting functions that have been proposed in the past for the DM velocity distribution. We adopt the following parameterizations of the DM velocity modulus distribution:
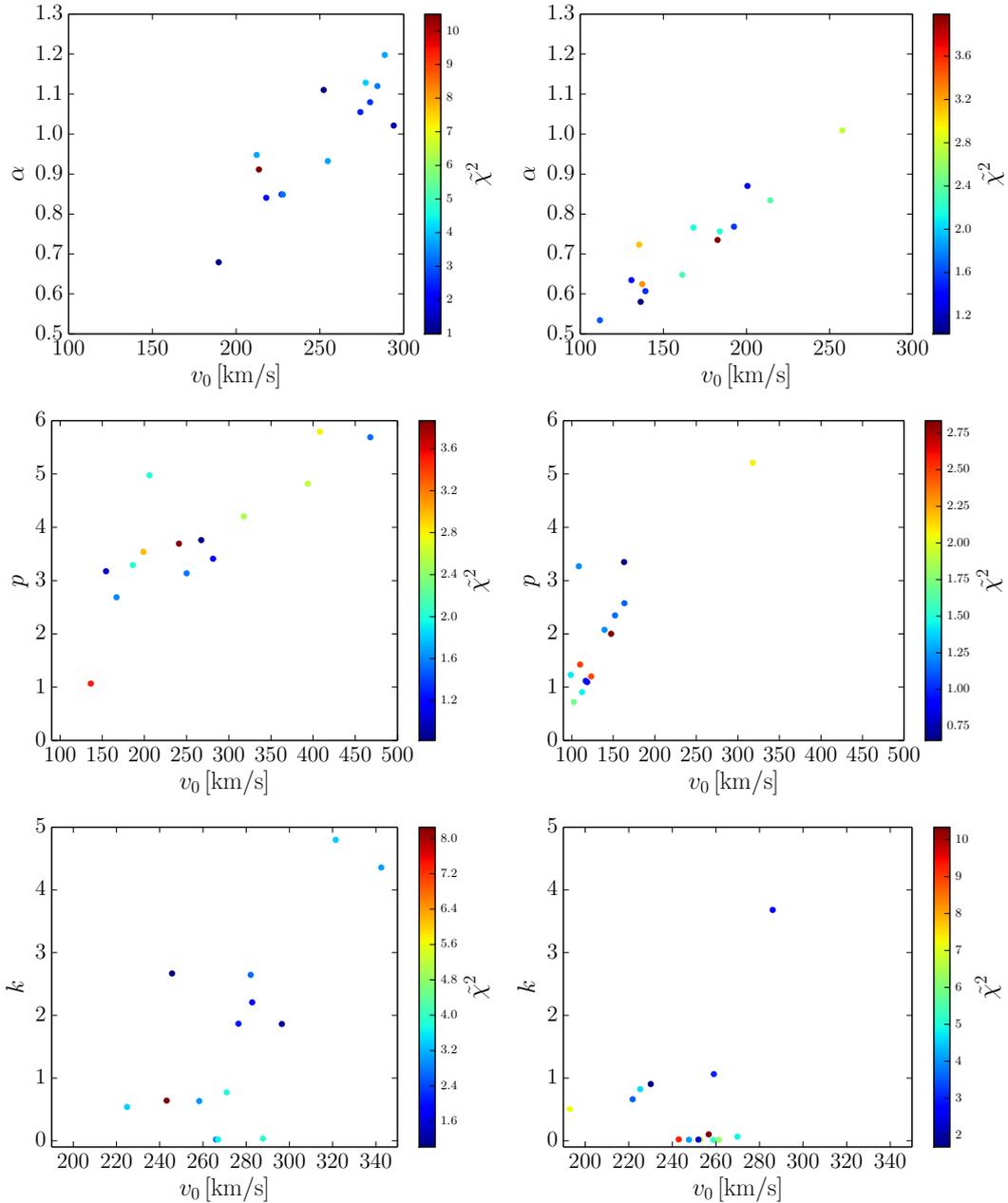
Figure 3. Left panels: Scatter plots showing the results of the fits to the simulated DM velocity modulus distribution for the set of 12 (EAGLE HR) + 2 (APOSTLE IR) selected MW-like galaxies when adopting, as fitting function, a generalized Maxwellian distribution (top panels), and the functions proposed in Mao *et al.* [33] (centre panels) and in Lisanti *et al.* [52] (bottom panels). The colour-bar corresponds to the value of the reduced χ^2, $\tilde{\chi}^2 \equiv \chi^2/(N - dof)$ (where $dof = 2$ for all three cases). Right panels: Same as left panels but for the corresponding haloes in the DMO simulations.

- Generalized Maxwellian distribution:

$$f(|\mathbf{v}|) \propto |\mathbf{v}|^2 \exp[-(|\mathbf{v}|/v_0)^{2\alpha}], \tag{4.2}$$

with free parameters v_0 and α. The case of a standard Maxwellian distribution is represented by $\alpha = 1$. We also test the goodness of fit for a standard Maxwellian to the simulated velocity modulus distributions (see tables 2 and 3 in Appendix C).

- The velocity modulus distribution proposed by Mao *et al.* [33]:

$$f(|\mathbf{v}|) \propto |\mathbf{v}|^2 \exp[-|\mathbf{v}|/v_0](v_{\text{esc}}^2 - |\mathbf{v}|^2)^p \, \Theta(v_{\text{esc}} - |\mathbf{v}|)\,, \qquad (4.3)$$

with free parameters v_0 and p.

- The velocity modulus distribution proposed by Lisanti *et al.* [52]:

$$f(|\mathbf{v}|) \propto |\mathbf{v}|^2 \exp[(v_{\text{esc}}^2 - |\mathbf{v}|^2)/(k\,v_0^2) - 1]^k \, \Theta(v_{\text{esc}} - |\mathbf{v}|)\,, \qquad (4.4)$$

with free parameters v_0 and k.

The normalisation of all the fitting functions is such that the 1D integral in velocity space of $f(|\mathbf{v}|)$ is equal to 1 (integrated from 0 to v_{esc}).

We perform the fit to the velocity modulus distributions of the simulated haloes with the above fitting functions, by minimising the χ^2 function:

$$\chi^2(\mathbf{p}) \equiv \sum_i^N \frac{(y_i - f(v_i, \mathbf{p}))^2}{\sigma_i^2}\,, \qquad (4.5)$$

where y_i is value of the velocity modulus distribution at the velocity v_i, σ_i is the corresponding 1σ Poisson error, N is the number of data points in the speed distribution (determined by the number of bins in speed which is $24 - 32$ depending on the halo in the hydrodynamic simulations), and $\mathbf{p}$ are the free parameters determined by the minimisation procedure. The local Galactic escape speed, v_{esc}, is a fixed parameter and as explained above it is determined for each simulated halo from the total mass enclosed in a sphere of radius 7 kpc, thus representing an upper limit on the escape speed at the Solar circle.

As can be seen from tables 2 and 3 in Appendix C, the Maxwellian distribution with a free peak ($\alpha = 1$ in eq. (4.2)) provides a better fit to most haloes in the hydrodynamic simulations compared to their DMO counterparts. However, the other fitting functions which have one extra free parameter in general provide a slightly better fit to haloes in both the hydrodynamic and DMO simulations. In particular, the Mao *et al.* function [33] provides the best fit for almost all haloes (except a few) for both the hydrodynamic and DMO cases.

In figure 3, we show the distribution of the best-fit parameters and compare the goodness of fit of the three fitting functions presented in eqs. (4.2), (4.3), and (4.4) for both hydrodynamic (left panels) and DMO simulations (right panels). In each panel the results are shown for the 12 EAGLE HR and 2 APOSTLE IR MW-like haloes. The function proposed by Mao *et al.* [33] (centre panels) fits both the hydrodynamic and DMO simulated haloes slightly better than the other fitting functions. There is no clear distinction in the goodness of fit values for DMO and hydrodynamic haloes. However, lower values for both the parameters p and v_0 are preferred by the DMO haloes, while the fit to the hydrodynamic counterparts spans a wider range in the parameter space.

The generalized Maxwellian distribution (top panels) provides a better fit to the DMO simulated haloes compared to the hydrodynamic haloes. This is due to the fact that the

local DM speed distributions of the DMO haloes are in general more symmetric around the peak than those obtained from the hydrodynamic haloes. Hence a generalized Maxwellian distribution can parametrize the speed distribution of the DMO haloes rather well. However, the DM speed distributions of the hydrodynamic haloes have more asymmetry in the high speed tail, and this is better described by the Mao *et al.* [33] fitting function. While DMO haloes prefer low α values ($0.5 - 1$) and low v_0 ($100 - 220$ km/s), most of the hydrodynamic haloes instead have larger best-fit parameters, α in the range $0.8 - 1.2$ and $v_0 > 190$ km/s. Analogous results are obtained when using the function proposed by Lisanti *et al.* [52] (bottom panels). For completeness, we list the best fit parameters and reduced χ^2 values for all fitting functions in Appendix C.

As we will discuss in section 6.2, the relevant quantity for predicting the event rates in direct detection experiments is the so-called "halo integral", which is the DM velocity distribution in the detector rest frame divided by the velocity and integrated over the DM velocity range relevant for direct detection. Since the halo integral is an integrated quantity, the local features and small fluctuations in the DM velocity distribution do not affect the halo integral strongly. However, large fluctuations and the position of the peak of the velocity modulus distribution are especially relevant for the halo integral. In particular, a larger peak speed of the velocity modulus distribution translates into a higher velocity tail of the halo integral. In section 6.2, we will discuss how the halo integral for the best fit Maxwellian velocity distribution for each halo compares to the halo integral computed directly from the simulation for our selected haloes.

4.2 Velocity distribution components

We next show the vertical, radial, and azimuthal components of the DM velocity distribution in the Galactic rest frame. Figures 4 and 5 show the DM velocity distribution components for the same two haloes shown in figure 2 in the EAGLE HR (haloes E3 and E12) and APOSTLE IR (haloes A1 and A2) hydrodynamic (left panels) and DMO (right panels) simulations, respectively.

It is clear from the three panels of figures 4 and 5 that the three components of the DM velocity distribution are not similar, and that there is a clear velocity anisotropy at the Solar circle. In particular, the radial speed distribution is broader than the vertical and tangential distributions in the hydrodynamic case. Another prominent feature visible in the bottom left panel of figure 4, is that the azimuthal component of the velocity distribution for halo E12 (shown in green) is skewed towards positive v_θ, indicating a significant rotation of the DM particles along the Galactic disc. Note that such a feature is not visible for the same halo in the DMO simulation (bottom right panel of figure 4). To quantify the features in the components of the DM velocity distribution for all the MW analogues, we fit them with the following fitting functions:

- A Gaussian function:

$$f(v_i) = \frac{1}{\sqrt{\pi} v_0} \exp\left[-(v_i - \mu)^2/v_0^2\right] , \qquad (4.6)$$

with free parameters v_0 and μ.

- A generalized Gaussian function:

$$f(v_i) = \frac{1}{2v_0\Gamma(1 + 1/(2\alpha))} \exp\left[-\left((v_i - \mu)^2/v_0^2\right)^\alpha\right], \qquad (4.7)$$

with free parameters v_0, μ, and α.

The functions are normalised such that the 1D integral in velocity space is equal to unity (integrated from $-\infty$ to $+\infty$).

Additionally, we fit the azimuthal component of the DM velocity distribution with a double Gaussian function:

$$f(v_\theta) = c_1 f_{1,\text{Gauss}}(v_\theta; v_1, \mu_1) + c_2 f_{2,\text{Gauss}}(v_\theta; v_2, \mu_2), \qquad (4.8)$$

with free parameters c_1, v_1, μ_1, v_2, and μ_2; c_2 is instead constrained by requiring $f(v_\theta)$ to be normalised to 1, $c_1 + c_2 = 1$.

In Appendix C, tables 4 and 5 we quote the best-fit parameters for the Gaussian and generalized Gaussian fits to the radial and vertical velocity components for the selected MW-like haloes in the EAGLE HR and APOSTLE IR hydrodynamic simulations. In tables 6 and 7, we present the best-fit parameters for the Gaussian, generalized Gaussian and double Gaussian fits for the azimuthal component of the DM velocity distribution. As for the distribution of the radial velocity component, v_r, the fit indicates that the distribution is well described by a generalized Gaussian with $\alpha \approx 1$ (close to the Gaussian function) and a mean radial velocity that is always smaller than ≈ 13 km/s (and for most of the haloes constrained between -5 km/s and +5 km/s). Analogous are the conclusions for the distribution of the vertical velocity component, v_z, which is generally peaked at values around $\mu = 0$ km/s. In the DMO counterparts of our selected haloes, both the radial and vertical velocity component distributions peak around zero as well. The distribution of the azimuthal velocity component, v_θ, is instead well fitted in most cases by either a Gaussian or a generalized Gaussian with an α parameter generally smaller than 1 (but larger than 0.6). The mean azimuthal speed is typically higher in the case of the hydrodynamic simulation than the mean radial and vertical speeds. In particular, 4 haloes in the EAGLE HR simulation (E4, E7, E10, E12) and 1 in the APOSTLE IR simulation (A1) have a significant non-zero mean azimuthal speed ($|\mu| > 20$ km/s). From these five haloes, 4 have positive mean speeds, while one halo is counter-rotating. When fitting the azimuthal velocity component with a generalized Gaussian, the same five haloes show evidence of rotation ($|\mu| > 3\sigma_\mu$).

To evaluate if baryonic processes are responsible for the net rotation of the DM particles in the tangential direction in the torus, we compare the azimuthal component of the velocity distribution for haloes in the hydrodynamic simulations with their counterparts in the DMO simulations. For the four haloes with positive mean azimuthal speeds with evidence of rotation in the hydrodynamic simulations, we find that their DMO counterparts do not show evidence of rotation at a comparable mean azimuthal speed. In particular, for these four haloes, the mean of the best fit generalized Gaussian for the azimuthal velocity component in the hydrodynamic case is larger than the corresponding mean in the DMO case, $\mu_{\text{hydro}} > \mu_{\text{DMO}} + 3\sigma_{\mu_{\text{DMO}}}$.

The asymmetry in the azimuthal component of the DM velocity distribution and the positive mean tangential speed observed for some haloes in the hydrodynamic simulations
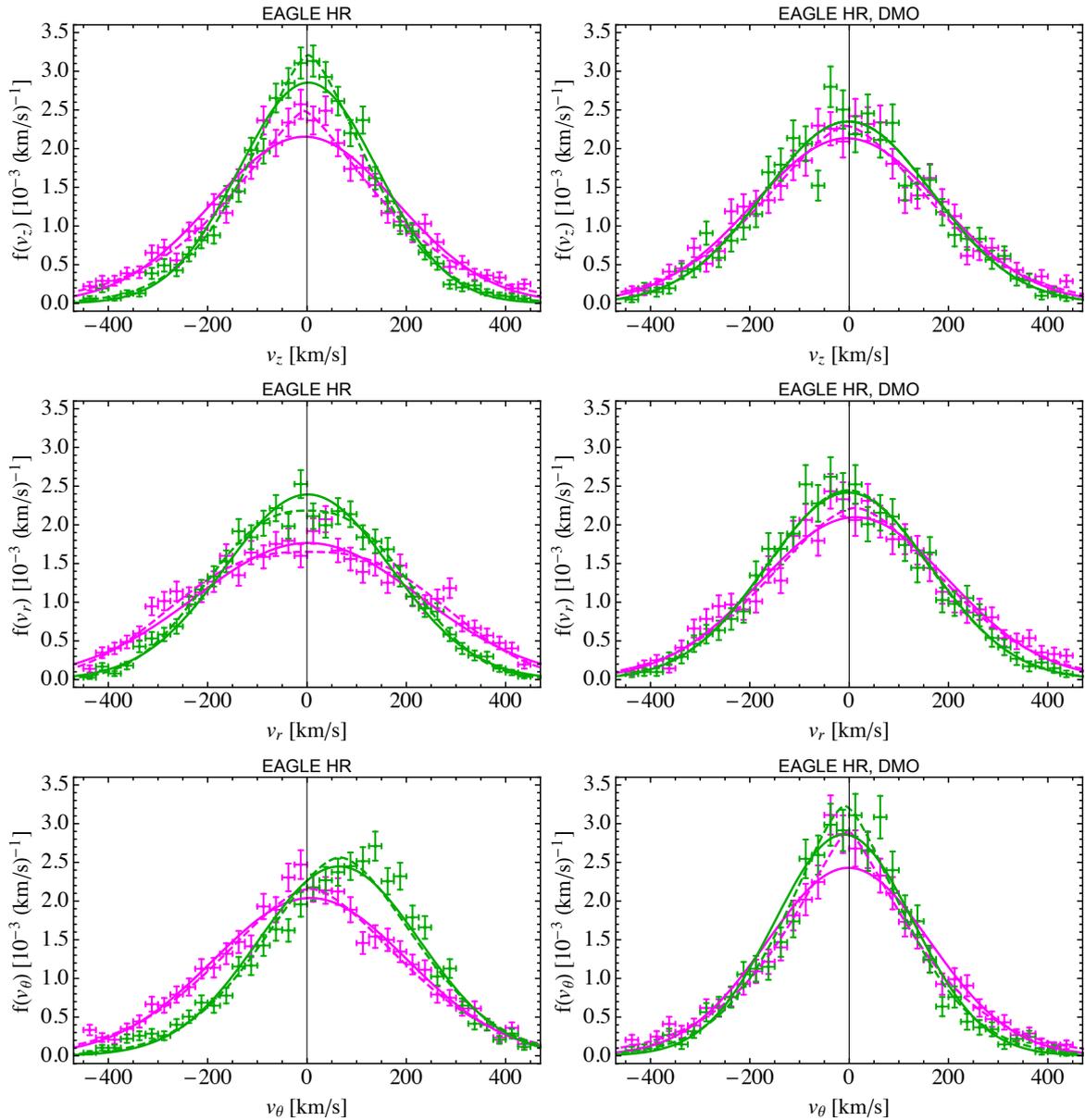
Figure 4. Left panels: The vertical (top panel), radial (middle panel), and azimuthal (bottom panel) components of the local DM velocity distribution in the Galactic rest frame (data points with 1σ error bars) for the two MW-like haloes in the EAGLE HR simulation which have the closest (halo E12, shown in green) and farthest (halo E3, shown in magenta) velocity modulus distribution compared to the SHM Maxwellian. The best fit Gaussian and generalized Gaussian distributions are also plotted as solid and dashed coloured lines, respectively. Right panels: Same as left panels but for the corresponding DMO simulation.

could be pointing to the existence of a "dark disc". The dark disc forms when the stars and gas in the Galactic disc drag merging satellite galaxies towards the Galactic plane. These satellites are then disrupted by tidal forces and their accreted material forms thick stellar and DM discs [54]. Previous hydrodynamic simulations by Read *et al.* [55] have found that
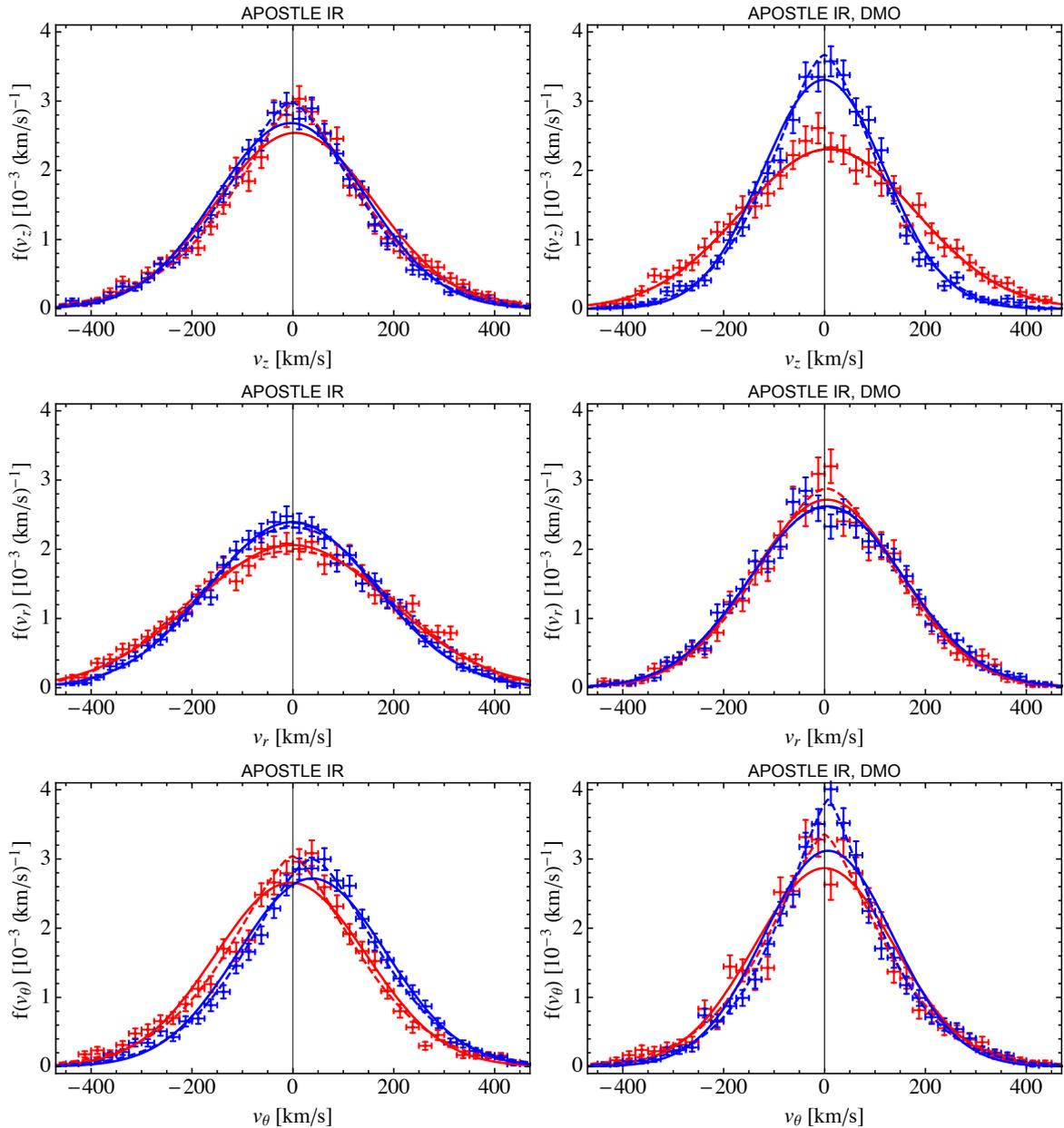
Figure 5. Same as figure 4 but for haloes A1 and A2 in the APOSTLE IR simulation.

the density of the dark disc can be $0.25 - 1.5$ times the halo density at $R_0 = 8$ kpc, and the rotation lag of the dark disc component is $0 - 150$ km/s compared to the stellar disc. Purcell *et al.* [56] found instead that the contribution of accreted DM material to the disc at the Solar position is less than $\approx 20\%$ of the host halo density, and the fraction of DM particles rotating with a lag velocity less than 50 km/s compared to the stellar disc is enhanced by less than $\approx 30\%$ compared to the SHM. The hydrodynamic simulation performed by Ling *et al.* [29] shows instead a dark disc component co-rotating with the Galactic disc which contributes $\approx 25\%$ of the total local DM density, and has a mean lag velocity of ≈ 75 km/s compared

to the stellar disc. For the Eris hydrodynamic simulation [32] the dark disc contributes 9.1% of the DM density in the disc. Ref. [32] quantifies the dark disc by computing the amount of material in the disc accreted from satellites with positive azimuthal velocities, co-rotating with the stellar disc.

We stress here that a large simulation sample may be necessary to draw robust conclusions regarding the dark disc, since large halo-to-halo scatter in the results is very likely. The conclusions may also be sensitive to stochastic effects and to the treatment of baryonic physics and so large samples, ideally drawn from simulations with different plausible baryonic physics, are needed to reach a definitive conclusion regarding the relevance of dark discs.

The implications of the dark disc for direct detection signals has been explored before [29, 32, 55–57]. Depending on the density of the dark disc, the event rates in direct detection experiments could be enhanced, especially in the low recoil energy range. The annual modulation signal and its phase could also be altered. In particular, depending on the lag velocity of the DM particles in the disc compared to the stellar particles, the phase of the annual modulation could be shifted. However, most previous simulations have shown that the increase in the local DM density due to the dark disc is relatively small [29, 32, 56] and therefore that direct detection signals do not change significantly due to the presence of a dark disc.

To assess whether a dark disc component might exist for any of our MW analogues, we extract the azimuthal velocity distribution of the star particles in the torus for each halo. We then fit the azimuthal components of both the DM and stellar velocity distributions with a double Gaussian. Our aim is to search for galaxies in which there is a DM component rotating as fast as the stars. Among the four haloes in our sample which show evidence of rotation with significant positive mean azimuthal speed, only two haloes (E7 and E12) have a rotating DM component in the disc with mean velocity comparable (within 50 km/s) to that of the stars. The azimuthal component of the DM velocity distribution for the same two haloes in the DMO simulation is symmetric around zero. Notice that both the E7 and E12 galaxies don't have a prominent stellar disc, as defined in ref. [39].

The two panels of figure 6 show the azimuthal components of the local DM (shown as black data points and 1σ error bars) and stellar (orange data points and 1σ error bars) velocity distributions for two MW-like haloes (E12 and E7) in the EAGLE HR simulation with comparable mean azimuthal velocities for the DM and stellar distributions. The left panel of figure 6 corresponds to the same halo (E12) as shown in the bottom left panel of figure 4. The black and orange solid lines show the best fit double Gaussian distribution to the DM and stellar azimuthal velocity distributions, respectively. We can see from the left panel that there are two kinematically distinct structures in the azimuthal component of the stellar velocity distribution in the torus centered at 8 kpc. The structure with a negative mean azimuthal speed contains most of the mass and is also present in a torus centered at 5 kpc as well as a torus centered at 10 kpc. While the structure with a positive mean azimuthal speed which contains less mass is not present at radii smaller than the Solar position, and may be due to the accretion of a massive satellite into the disc region. Hence, this structure is likely a "ring" of stars, the relic of a "ring" of gas that accretes late in the formation of the galaxy. Such features are not infrequent in simulations of galaxy formation (see e.g. [58]).

In the left (right) panel of figure 6, when fitting with a double Gaussian distribution, the mean azimuthal velocity for the second Gaussian (with higher μ) is 136 km/s (88 km/s) for the
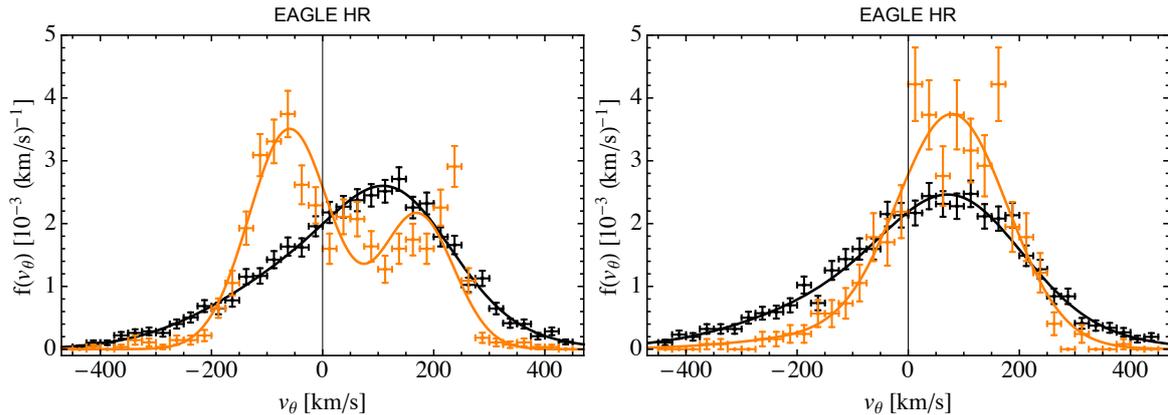
Figure 6. Azimuthal components of the local DM (black data points with 1σ error bars) and stellar (orange data points with 1σ error bars) velocity distribution in the Galactic rest frame for the two MW-like haloes in the EAGLE HR simulation which have comparable peaks at positive azimuthal speeds v_θ. Left panel: halo E12; right panel: halo E7. The best fit double Gaussian distributions to the DM and stellar distributions are also plotted as solid black and orange lines, respectively.

DM distribution, and 171 km/s (81 km/s) for the stellar distribution. Thus, the differences in the second peak of the double Gaussian between the DM and stellar distributions are 35 km/s and 7 km/s, in the left and right panels, respectively. The fraction of the rotating component of the double Gaussian DM distribution with the larger mean velocity is 32% and 43% in the left and right panels, respectively.

In summary, from a total of 14 MW-like haloes in our sample, evidence for a significant positive mean azimuthal speed, which is comparable for DM and stars in the torus, exists only for two haloes, and this may hint at the existence of a co-rotating dark disc in those two haloes. Although the mechanism that has been proposed to produce a dark disc may be causing the features discussed for these two haloes, to draw such a conclusion one would need to follow the accretion history of massive satellites into the disc region, and this is beyond the scope of this paper. One instead can conclude that even in the case that the dark disc is responsible for such features, this is a relatively rare occurrence in our halo sample, occurring only in two out of 14 haloes. Notice also that the selection of our MW-like halo sample is unbiased with respect to the formation of a dark disc.

5   Local dark matter density and halo shape

The fiducial value of the local DM density in the SHM is 0.3 GeV/cm^3. By considering a large range of halo profiles and by constraining the mass model of the MW using global dynamical data sets, local DM densities in the range of (0.2 – 0.6) GeV/cm^3 are obtained [49, 59–64]. Local estimates of the DM density [65–70] are consistent with the global estimates, although they have larger uncertainties.

Here we extract the local DM density using the torus discussed in section 4. The average local DM density in the torus is $0.42 - 0.73$ GeV/cm^3 for the 12 haloes in the EAGLE HR simulation, and $0.41 - 0.54$ GeV/cm^3 for the two haloes in the APOSTLE IR simulation. When splitting the torus into smaller angular regions (8 regions for EAGLE HR, and 16 regions for

APOSTLE IR), we find that the average DM density varies on average by 32% along the torus, a variation smaller than the halo-to-halo scatter. Notice that the values we find for the local DM density are in agreement with the global and local estimates discussed above.

To determine if there is an enhancement of the local DM density in the Galactic disc compared to the halo, we compare the average value of the local DM density in the torus with the average value in a spherical shell at $7 < R < 9$ kpc. The average DM density in the shell is in the range $0.41 - 0.66$ GeV/cm^3 for the MW-like haloes in the EAGLE HR simulation, and is 0.42 GeV/cm^3 for the two APOSTLE IR MW analogues. From the 14 MW analogues in both simulations (12 in EAGLE HR + 2 in APOSTLE IR), the local DM density is higher by $2 - 27\%$ for 10 haloes compared to the shell averaged value, while the enhancement is greater than 10% for five haloes, and greater than 20% for only two haloes. To evaluate if baryonic physics is responsible for this enhancement, we compare the average local DM density in an identical torus and shell for the same haloes in the DMO simulations. We find that two of the DMO counterparts (haloes E1 and E11) show a similar increase of the DM density in the torus compared to the shell, which can be due to the halo itself not being a perfect sphere.

The increase in the local DM density in the disc for some haloes could be due to the DM halo contraction as a result of dissipational baryonic processes in the hydrodynamic simulations (See [71] for a measure of dark halo contraction in the EAGLE galaxy formation model). Note that for the two haloes discussed in section 4.2 which have a DM component co-rotating with the stellar disc with a mean azimuthal speed comparable to that of the stars, the local DM density in the Galactic disc is 27% higher for halo E12 (shown in the left panel of figure 6) and 9% lower for halo E7 (shown in the right panel of figure 6) compared to the shell averaged value.

To further understand the effect of baryonic physics on the local DM density, we can study the shape of the inner (< 8 kpc) DM halo. We first calculate the inertia tensor of the DM particles within two different radii (5 kpc and 8 kpc). The resulting inertia tensor then describes an ellipsoid with three axes of length $a \geq b \geq c$: these lengths provide information about the shape of the DM distribution. We also repeat this process for the DMO counterparts to our EAGLE HR galaxy sample.

We first calculate the sphericity, $s = c/a$. If the DM distribution is a perfect sphere, all three axes will have the same length, so $c = a$ and thus sphericity $s = 1$; a value of $s < 1$ describes an increasing deviation from sphericity in our sample. We find for our galaxy sample that the sphericities at 5 kpc cluster in the range $s = [0.85, 0.95]$ and are typically lower by less than 10% at 8 kpc, thus haloes have a larger deviation from a sphere at larger radii. In both cases, however, due to dissipational baryonic processes the DM sphericity is systematically higher in the hydrodynamic simulations than is the case for the DMO runs, in which the range in s is $[0.75, 0.85]$. This result is in agreement with earlier detailed simulations [72, 73] and reproduces what was found in higher resolution simulations of the APOSTLE series [74].

Where there is a deviation from sphericity, this can be described using the triaxiality parameter, T, which is defined as

$$T = \frac{a^2 - b^2}{a^2 - c^2}. \tag{5.1}$$

For very oblate systems, $a \approx b \gg c$ and thus $T \approx 0$, whereas for the opposite, prolate case $a \gg b \approx c$ and $T \approx 1$. We find that there is little correlation in our galaxy sample

between the values of T at 5 kpc and 8 kpc, with both varying in the range $[0.02, 0.8]$. However, it should be noted that because these inner haloes are very close to spherical ($s = [0.81, 0.96]$), the deviation towards either prolate or oblate distributions is very small. By contrast, the DMO counterparts almost all have a preference for inner haloes that are prolate rather than oblate, with $T = [0.4, 0.9]$ at both radii for all of our candidates. We therefore conclude that spherical symmetry is a very good approximation for our galaxy halo centres with little dependence on radius, and that this marks an important difference from DMO studies.

For halo E12 (shown in the left panel of figure 6), which has a local DM density in the torus enhanced by 27% compared to the shell averaged value, the triaxiality parameter $T = 0.02$ at 8 kpc, which implies an oblate halo, as expected.

6 Direct detection signals

6.1 Event rates

We consider a DM particle χ scattering elastically off a nucleus with atomic mass number A and atomic number Z, and depositing the nuclear recoil energy E_R in the detector. The differential rate (events per unit energy, per unit detector mass, per unit time) is given by

$$\frac{dR}{dE_R} = \frac{\rho_\chi}{m_\chi} \frac{1}{m_A} \int_{v > v_{\min}} d^3v \frac{d\sigma_A}{dE_R} v \tilde{f}_{\det}(\mathbf{v}, t). \tag{6.1}$$

Here ρ_χ is the local DM density, m_χ and m_A are the DM and nucleus masses, σ_A is the DM–nucleus scattering cross section and $\mathbf{v}$ is the 3-vector relative velocity between DM and the nucleus, while $v \equiv |\mathbf{v}|$. $\tilde{f}_{\det}(\mathbf{v}, t)$ is the DM velocity distribution in the detector rest frame normalised to unity, such that $\int d^3v \tilde{f}_{\det}(\mathbf{v}, t) = 1$. For the case of elastic scattering, the minimum speed $v_{\min}$ required for a DM particle to deposit a recoil energy E_R in the detector is given by

$$v_{\min} = \sqrt{\frac{m_A E_R}{2\mu_{\chi A}^2}}, \tag{6.2}$$

where $\mu_{\chi A} = m_\chi m_A / (m_\chi + m_A)$ is the reduced mass of the DM and nucleus.

The differential cross section is in general a sum of spin-independent and spin-dependent contributions. Here we only consider the case of spin-independent scattering and assume equal couplings of DM to protons and neutrons. In this case the differential cross section is

$$\frac{d\sigma_A}{dE_R} = \frac{m_A A^2}{2\mu_{\chi p}^2 v^2} \sigma_{\mathrm{SI}} F^2(E_R), \tag{6.3}$$

where σ_{SI} is the spin-independent DM–nucleon scattering cross section, $\mu_{\chi p}$ is the reduced mass of the DM–nucleon system, and $F(E_R)$ is a form factor for which we use the expression from Helm [75].

The DM velocity distribution is usually given in the Galactic rest frame, and to calculate the event rate in Eq. (6.7), one has to transform the velocity distribution from the Galactic rest frame to the rest frame of the detector, by

$$\tilde{f}_{\det}(\mathbf{v}, t) = \tilde{f}_{\mathrm{gal}}(\mathbf{v} + \mathbf{v}_s + \mathbf{v}_e(t)), \tag{6.4}$$

where $\mathbf{v}_e(t)$ is the velocity of the Earth with respect to the Sun, and $\mathbf{v}_s = \mathbf{v}_c + \mathbf{v}_{\rm pec}$ is the velocity of the Sun in the Galactic rest frame. Here $\mathbf{v}_c$ is the Sun's circular velocity (or Local Standard of Rest (LSR) velocity), and $\mathbf{v}_{\rm pec} \approx (11.10, 12.24, 7.25)$ km/s [76] is the peculiar velocity of the Sun with respect to the LSR. For each simulated halo, we set $\mathbf{v}_c = (0, v_\star, 0)$, where $v_\star$ is the local circular speed for that halo, rather than using the fiducial value of $(0, 230, 0)$ km/s for the Sun's circular velocity. The velocities are given in Galactic coordinates where the x-axis points towards the Galactic centre, the y-axis points in the direction of the Galactic rotation, and the z-axis points to the North Galactic pole.

The velocity of the Earth with respect to the Sun, $\mathbf{v}_e(t)$, causes the time dependence of the differential event rate, and can be written as [77]

$$\mathbf{v}_e(t) = v_e[\mathbf{e}_1 \sin \lambda(t) - \mathbf{e}_2 \cos \lambda(t)], \tag{6.5}$$

assuming a circular orbit. Here $v_e = 29.8$ km/s is the orbital speed of the Earth, and $\lambda(t) = 2\pi(t-0.218)$ with t in units of 1 year and $t = 0$ on January 1st. The orthogonal unit vectors $\mathbf{e}_1$ and $\mathbf{e}_2$ span the plane of the Earth's orbit, and are given by, $\mathbf{e}_1 = (-0.0670, 0.4927, -0.8676)$ and $\mathbf{e}_2 = (-0.9931, -0.1170, 0.01032)$ in Galactic coordinates. For simplicity, we neglect the small eccentricity of the Earth's orbit since Eq. (6.5) provides an excellent approximation to describe the annual modulation signal [78].

6.2 Halo integral

The astrophysical uncertainties in the event rate originate from the uncertainties in the DM velocity distribution and density at the position of the Sun. Let us define the halo integral as

$$\eta(v_{\rm min}, t) \equiv \int_{v > v_{\rm mim}} d^3v \frac{\tilde{f}_{\rm det}(\mathbf{v}, t)}{v} . \tag{6.6}$$

Then from Eqs. 6.1 and 6.3, the differential event rate can be written as

$$\frac{dR}{dE_R} = \frac{\rho_\chi A^2 \sigma_{\rm SI}}{2m_\chi \mu_{\chi p}^2} F^2(E_R) \eta(v_{\rm min}, t). \tag{6.7}$$

The halo integral $\eta(v_{\rm min}, t)$, together with the local DM density ρ_χ, encapsulates the astrophysics dependence of the event rate.

The top left panel of figure 7 shows the time averaged halo integral as a function of the minimum velocity, $v_{\rm min}$, for the two haloes with speed distributions that are the closest to (halo E12), and the farthest from (halo E3), the SHM Maxwellian (specified with a solid black line) in the set of EAGLE HR MW-like galaxies. The bottom left panel of the same figure shows the time averaged halo integral for the two APOSTLE IR MW-like haloes. The right panels show the halo integral for the same haloes in the left panels but in a DMO simulation. The coloured solid lines specify the halo integral computed from the mean value of the velocity distribution, while the shaded band is obtained by adding and subtracting one standard deviation to the mean velocity distribution. The halo integrals obtained from the best fit Maxwellian velocity modulus distributions (eq. (4.2) with $\alpha = 1$) are shown by dashed coloured lines with matching colours for each halo.

From the left panels of figure 7, one can see that the halo-to-halo scatter in the halo integral is significant. There are MW-like haloes which have halo integrals similar to the
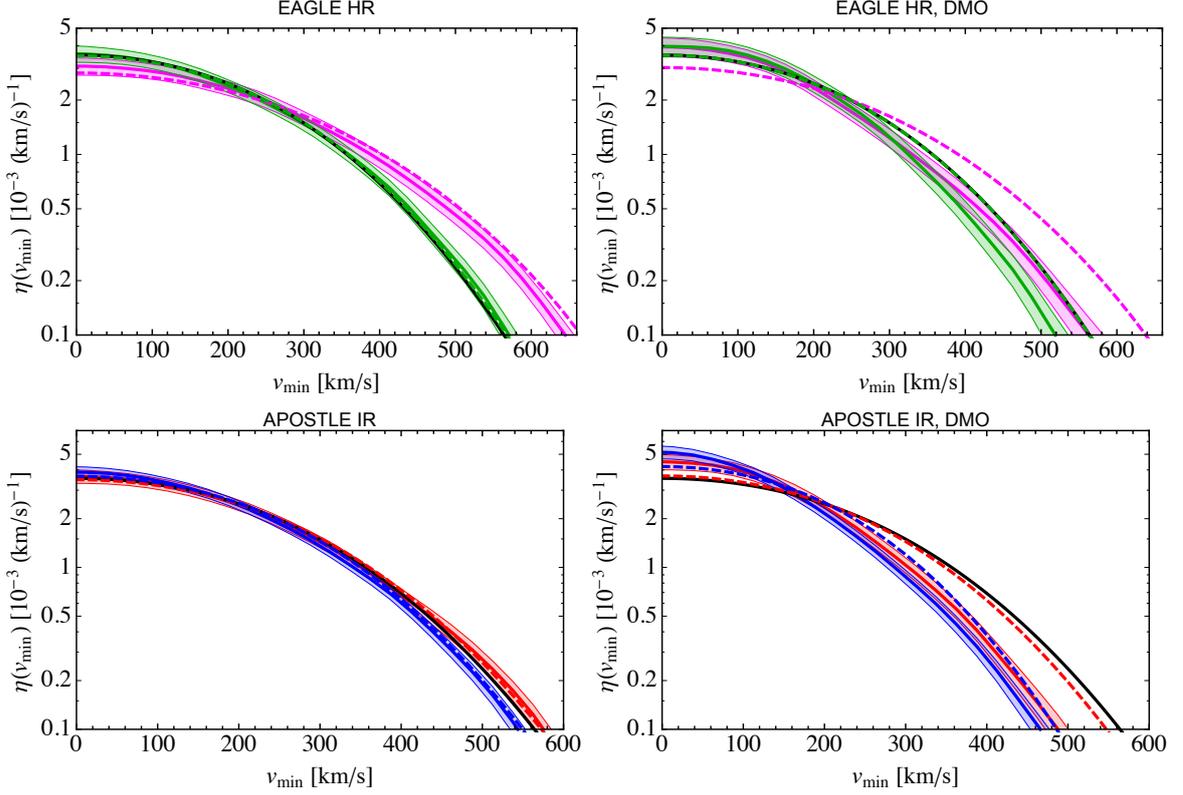
Figure 7. Time averaged halo integrals (solid coloured lines) for the the two haloes closest to (halo E12 shown in green) and farthest from (halo E3 shown in magenta) the SHM Maxwellian in the EAGLE HR simulation (top left), and the two haloes (blue and red lines) in the APOSTLE IR simulation (bottom left). The solid coloured lines and the shaded bands correspond to the halo integrals obtained from the mean velocity distribution and the velocity distribution at $\pm 1\sigma$ from the mean, respectively. The solid black line specifies the halo integral for the SHM Maxwellian (with peak speed of 230 km/s), and the dashed coloured lines specify the halo integral obtained from the best fit Maxwellian velocity modulus distribution for each halo (with matching colours). The right panels show the halo integrals for the same haloes in the corresponding left panel but in a DMO simulation.

SHM Maxwellian, but there also exists MW analogues with halo integrals that deviate from the SHM Maxwellian significantly at higher minimum velocities. The effect is more evident for the EAGLE HR sample, for which we have more haloes. Comparing to the DMO case, where the halo-to-halo scatter is less pronounced, one can conclude that baryons affect the velocity distribution strongly at $R_0 = 8$ kpc, typically resulting in a shift of the tails of the halo integral to higher velocities with respect to the DMO case.

The difference between the halo integral of the simulated haloes in the hydrodynamic case and the SHM Maxwellian, which is more pronounced at relatively large $v_{\min}$, is mainly due to the different peak speed of the DM velocity distribution of the simulated haloes compared to the 230 km/s assumed for the SHM Maxwellian. Indeed, the halo integral for the best fit Maxwellian velocity distribution falls within the 1σ uncertainty band of the halo integrals for all but two MW-like haloes in the hydrodynamic simulation. For those two haloes, there is only a slight deviation between the halo integral for the best fit

Maxwellian and the simulated halo at large v_{min}. The range of the best fit v_0 parameter for the Maxwellian distribution is 223 – 289 km/s in the hydrodynamic case, as can be seen in table 2 in Appendix C.

On the other hand, the shape of the DM velocity modulus distributions for the haloes in the DMO simulations are not well captured by the Maxwellian distribution with a free peak. For most haloes in the DMO case, there are large deficits at the peak, and an excess of particles at low and very high velocities compared to the best fit Maxwellian speed distribution. These large differences result in halo integrals of the simulated haloes which are quite different from the best fit Maxwellian halo integrals, as can be seen from the right panels of figure 7.

7 Results

We discuss below the details of the analysis of direct detection data using directly the local DM density and velocity distribution of the selected MW analogues. Our aim is to investigate how the allowed regions and exclusion limits set by different direct detection experiments in the plane of DM mass and spin-independent cross section change for our selected haloes compared to the SHM, and if the compatibility between the hints for a DM signal and null-results improves.

7.1 Data from direct detection experiments

In this section we discuss our analysis of the data from multiple direct detection experiments. In particular, we consider the positive signals from DAMA/LIBRA [1] (DAMA for short) and the silicon detectors in CDMS-II [2] (CDMS-Si for short), as well as the the null-results from the LUX [3] and SuperCDMS [4] experiments.

DAMA: The DAMA experiment observed an annual modulation signal at the 9.3σ level over 14 annual cycles. We use the data on the annual modulation amplitude given in figure 8 of ref. [1] for the total cumulative exposure of 1.33 ton yr of DAMA/LIBRA-phase1 and DAMA/NaI. In our analysis, we consider 12 bins in the signal region between 2 keVee and 8 keVee, above which the data is consistent with zero modulation. For the quenching factors of Na and I, we use $q_{\text{Na}} = 0.3$ and $q_{\text{I}} = 0.09$, respectively, as measured by the DAMA collaboration [79].

Our analysis of the DAMA data is similar to the analyses in [80–82]. In particular, we construct a χ^2 function to fit the DAMA data,

$$\chi^2_{\text{DAMA}}(m_\chi, \sigma_{\text{SI}}) = \sum_{i=1}^{i=12} \left(\frac{A_i^{\text{pred}}(m_\chi, \sigma_{\text{SI}}) - A_i^{\text{obs}}}{\sigma_i} \right)^2, \tag{7.1}$$

where the sum is over the 12 energy bins, A_i^{pred} is the predicted annual modulation amplitude, while A_i^{obs} and σ_i are the experimental data points and their errors, respectively, from figure 8 of ref. [1]. To find the best fit, we minimize Eq. (7.1) with respect to the DM mass m_χ, and spin-independent DM–nucleon cross section σ_{SI}. The allowed regions in the $m_\chi - \sigma_{\text{SI}}$ plane at a given CL are obtained from contours of $\chi^2(m_\chi, \sigma_{\text{SI}}) = \chi^2_{\text{min}} + \Delta\chi^2(\text{CL})$, where $\Delta\chi^2(\text{CL})$ is evaluated for 2 degrees of freedom (dof), e.g., $\Delta\chi^2(99.73\%) = 11.8$ and $\Delta\chi^2(90\%) = 4.6$.

CDMS-Si: Three DM candidate events with recoil energies of 8.2, 9.5, and 12.3 keV were observed in the 140.2 kg day of data taken with the Si detectors of the CDMS-II experiment [2]. The total estimated background was 0.62 events in the recoil energy range of $[7, 100]$ keV. Our analysis of the CDMS-Si data is analogous to the one presented in refs. [21, 83]. To include the background, we rescale the individual background spectra from ref. [84], such that 0.41, 0.13, and 0.08 events are expected from surface events, neutrons, and ^{206}Pb, respectively. We assume an energy resolution of 0.3 keV and use the detector acceptance from ref. [2].

LUX: The LUX experiment has presented the analysis of 85.3 live-days of data [3], which is consistent with the background-only hypothesis. Assuming the SHM, the LUX result is in strong tension with positive hints from DAMA and CDMS-Si. We use the maximum gap method [85] to set exclusion limits, since with the available information we cannot reproduce the likelihood analysis performed by the LUX collaboration. We consider the region below the mean of the Gaussian fit to the nuclear recoil calibration events (red solid curve in figure 4 of [3]) as signal region, and assume an acceptance of 0.5. Figure 4 of [3] shows that one event at 3.1 photoelectrons falls on the red solid curve. Hence, in this analysis we assume zero events make the cut. To find the relation between S1 and nuclear recoil energy E_R, we use figure 4 of [3] and find the value of S1 at the intersection of the mean nuclear recoil curve and each recoil energy contour. For the efficiency as a function of recoil energy, we interpolate the black points in figure 9 of [3] for events with a corrected S1 between 2 and 30 photoelectrons and a S2 signal larger than 200 photoelectrons. We multiply the efficiency from figure 9 of [3] by 0.5 to find the total efficiency, and set it equal to zero below $E_R = 3$ keV. Assuming the SHM with the Maxwellian velocity distribution and parameters chosen as in [3], the 90% CL exclusion limit we find agrees well with the limit set by the LUX collaboration.

SuperCDMS: Eleven events in the recoil energy range of [1.6, 10] keV have been observed by the SuperCDMS collaboration with an exposure of 577 kg day of data taken with their Ge detectors [4]. The collaboration sets a 90% CL on the spin-independent DM–nucleon cross section of 1.2×10^{-42} cm^2 at a DM mass of 8 GeV. We employ the maximum gap method to set an upper limit on the cross section. We use the red curve in figure 1 of [4] for the detection efficiency as a function of recoil energy, and assume an energy resolution of 0.2 keV.

7.2 Dark matter parameter space

In this section, we present our results for the exclusion limits and allowed regions in the DM mass and interaction cross section plane set by each direct detection experiment discussed in section 7.1 when assuming the DM distribution of the simulated MW-like galaxies. Notice that we use directly the local DM density and velocity distributions extracted from the simulations to perform the analysis of direct detection data.

To illustrate the effect of baryons on the interpretation of direct DM detection results, we consider four benchmark haloes in the EAGLE HR hydrodynamic simulation which satisfy our selection criteria: two haloes with the smallest (halo E6) and largest (halo E4) local DM densities, and two haloes with speed distributions closest to (halo E12) and farthest from (halo E3) the SHM Maxwellian. The exclusion limits and allowed regions in the m_χ–$\sigma_{\rm SI}$ plane obtained assuming the DM distribution of these benchmark haloes encompass the

range of results obtained assuming the DM distribution of all our MW-like analogues. For the APOSTLE IR simulation, we present the results for the two haloes which satisfy our selection criteria (haloes A1 and A2).

The top panels of figure 8 show the allowed regions from the DAMA and CDMS-Si experiments and exclusion limits from the LUX and SuperCDMS experiments in the plane of DM mass and spin-independent cross section for these four EAGLE HR benchmark haloes. In the left panel, the results are shown for the two haloes with smallest (E6) and largest (E4) ρ_χ, whereas in the right panel the results are shown for the two haloes with speed distributions closest to (E12) and farthest from (E3) the SHM Maxwellian. The bottom panel shows the results for the same two haloes in the top right panel (E3 and E12), but setting the local DM density to 0.3 GeV/cm³ for both haloes, in order to isolate the effect induced by the deviation of the velocity distribution from the SHM Maxwellian distribution.

For comparison, the allowed regions and exclusion limits assuming the SHM Maxwellian (with peak speed of 230 km/s) velocity distribution and a local DM density of 0.3 GeV/cm³ are shown in black. The shaded band in the exclusion limits and the two allowed regions of the same colour are obtained from the upper and lower 1σ limits of the halo integrals.

One can see from figure 8 that the general vertical shift of the preferred regions and exclusion limits with respect to the SHM at all DM masses is due to the variation in the local DM density, whereas the shift at low DM masses is due to the high velocity tail of the DM distribution. For the halo with speed distribution farthest from the SHM Maxwellian (E3) and assuming a local DM density of 0.3 GeV/cm³, the allowed regions and exclusion limits at low DM masses ($m_\chi \leq 10$ GeV) shift by a maximum of ~ 2 GeV towards smaller DM masses (bottom panel of figure 8). When considering the local DM density extracted from simulations for each halo, all the regions and exclusion limits shift vertically at most by a factor of $\sim 2 - 3$ in the scattering cross section compared to the SHM (see left panel of figure 8). This vertical shift is due to the different local DM densities of the simulated haloes compared to the SHM, which enters as a normalisation factor in the predicted recoil rate in direct detection experiments.

It is also clear from figure 8 that the halo-to-halo scatter is larger than the 1σ uncertainty for each halo. Notice also that in general the preferred regions and exclusion limits all shift in the same direction, and thus the compatibility between the results of different experiments is not improved for any of the simulated haloes.

The left panel of figure 9 is the same as the top left panel of figure 8, but for the two APOSTLE IR haloes (A1 and A2). The right panel shows the results for the same two haloes in the left panel but assuming a fixed local DM density of 0.3 GeV/cm³ for both haloes. The same features discussed for the EAGLE HR haloes are also visible for the APOSTLE IR haloes in figure 9.

8 Conclusions

In this work we have studied the predictions of the set of cosmological, hydrodynamic simulations of the EAGLE [35, 36] and APOSTLE [37, 38] projects for DM direct detection. Considering first all simulated haloes in the mass range $\mathcal{O}(10^{12} - 10^{13})\,\mathrm{M}_\odot$, we applied two selection criteria for choosing galaxies that are MW-like: (i) the rotation curve of the simulated galaxy provides a good fit to the recent compilation of observed MW rotation curves from ref. [5],
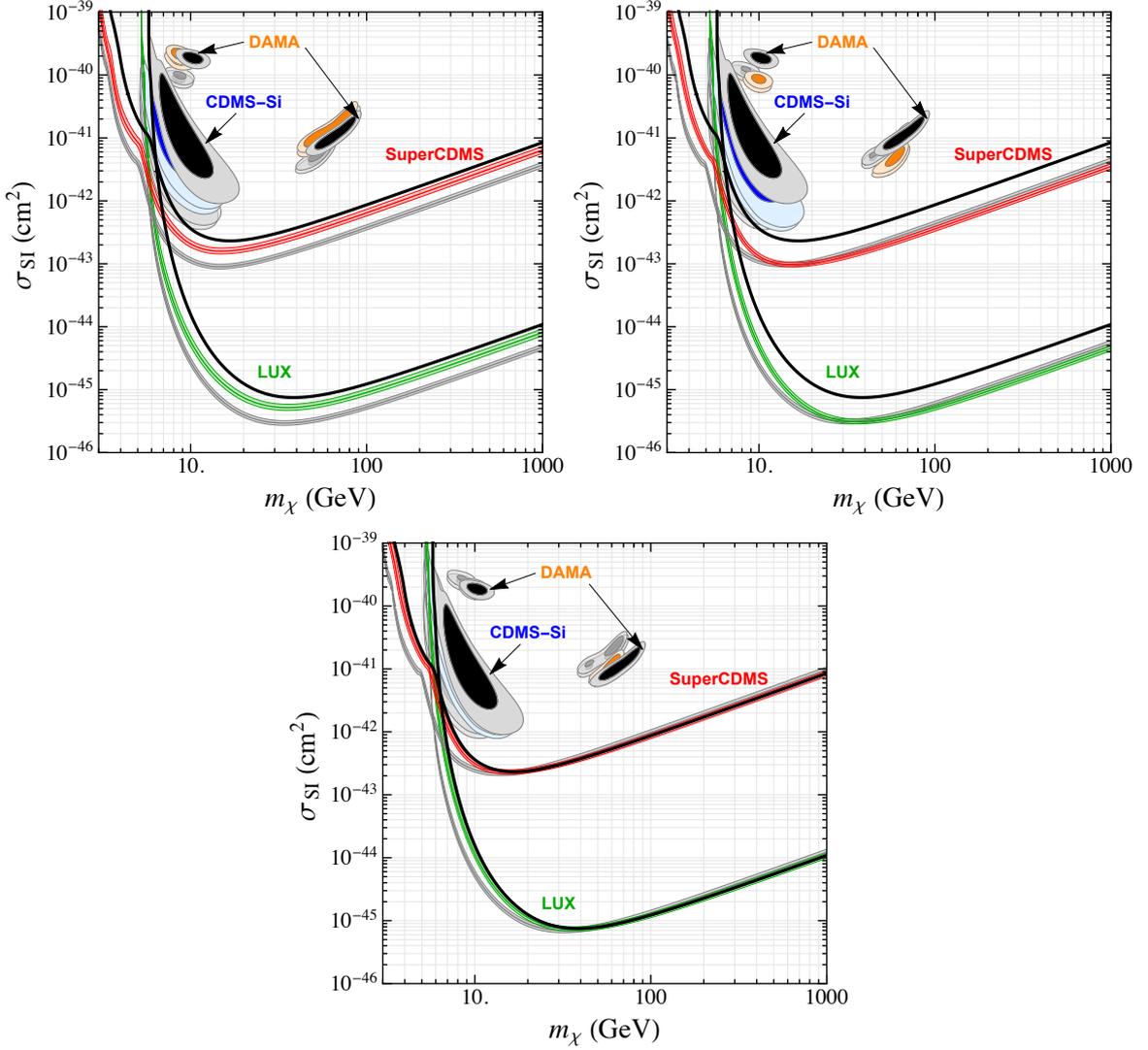
Figure 8. Exclusion limits from LUX and SuperCDMS (at 90% CL) and preferred regions from DAMA (at 90% CL and 3σ) and CDMS-Si (at 68% and 90% CL) in the spin-independent DM–nucleon cross section and DM mass plane for two haloes in the EAGLE HR run with the smallest (halo E6 shown in colour) and largest (halo E4 shown in gray) ρ_χ (top left panel), and two haloes with velocity distributions closest to (halo E12 shown in colour) and farthest from (halo E3 shown in gray) the SHM Maxwellian (top right panel). The bottom panel shows the results for the same two haloes in the top right panel (E3 and E12) but assuming $\rho_\chi = 0.3$ GeV/cm³ for the two haloes instead of using the ρ_χ for each halo from the simulations. The shaded bands in the exclusion limits and the two adjacent allowed regions of the same colour are obtained from the upper and lower 1σ limits of the halo integral for each halo. The black exclusion limits and allowed regions correspond to the SHM Maxwellian. The local ρ_χ is 0.42 and 0.73 GeV/cm³ for the two haloes in the top left panel, and it is 0.68 and 0.71 GeV/cm³ for the two haloes in the top right and bottom panels.

and (ii) the stellar mass of the simulated galaxy is within the 3σ observed stellar mass range of the MW, $4.5 \times 10^{10} < M_*/\mathrm{M}_\odot < 8.3 \times 10^{10}$ [49]. We have shown that these two selection
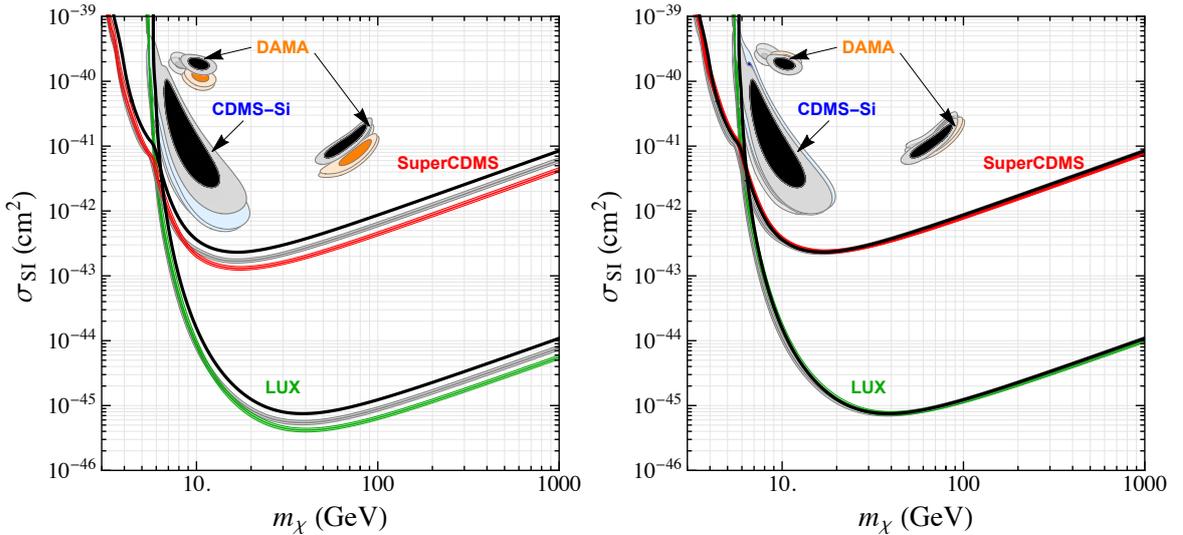
Figure 9. Same as figure 8 but for the two selected haloes (A1 and A2) in the APOSTLE IR simulation. Left panel: Using the ρ_χ for each halo (0.41 and 0.54 GeV/cm^3) from the simulations. Right panel: Assuming $\rho_\chi = 0.3$ GeV/cm^3 for both haloes.

criteria are especially relevant for accurate predictions of the local DM density and velocity distribution, which are important quantities for investigating the implications for DM direct detection searches.

For our selected MW analogues (12 EAGLE HR and 2 APOSTLE IR), we extracted the DM distributions and used them directly to perform an analysis of current dark matter direct detection experiments data. In particular, we studied the implications of the simulated MW-like haloes for direct detection considering the allowed regions from DAMA [1] and CDMS-Si [2] and exclusion limits from LUX [3] and SuperCDMS [4] assuming spin-independent elastic scattering. We summarize our main findings below:

- Including baryons in the hydrodynamic simulations results in a shift of the local DM velocity distributions to larger velocities compared to the DMO simulations. This results in a shift in the tails of the halo integral (eq. (6.6)) to higher velocities in the hydrodynamic compared to the DMO simulations.

- The halo integrals obtained from the best fit Maxwellian velocity distribution for each halo fall within the 1σ uncertainty band of the halo integrals obtained directly from the simulated velocity distributions for all but two MW-like haloes in the hydrodynamic simulations. The range of the best fit peak speed for the Maxwellian velocity distribution is 223 – 289 km/s. The deviation in the best fit peak speed values from the SHM Maxwellian results in a shift of the halo integral tail at large velocities.

- Anisotropy in the DM velocity distribution is present at the Solar circle. In particular, four haloes in our sample show evidence of rotation with significant positive mean azimuthal speed ($\mu > 20$ km/s), but only two of them have comparable mean azimuthal

speeds for DM and star particles. This may be hinting towards the existence of a dark disc for two out of 14 MW analogues.

- The average local DM density in a torus aligned with the stellar disc and at 7 kpc < R < 9 kpc and $|z|$ < 1 kpc is $0.41 - 0.73$ GeV/cm^3 for our halo sample. Most haloes in our sample show an enhancement of the local DM density in the torus compared to the spherical shell at the Solar circle (with 7 kpc < R < 9 kpc). In particular, the local DM density in the torus is enhanced by more than 10% for five haloes, and by more than 20% for two haloes compared to the shell-averaged value. Haloes in the hydrodynamic simulation are in general more spherical compared to the DMO case. However, they are not perfect spheres, and are typically slightly more oblate compared to their DMO counterparts.

- The variation in the local DM density from halo-to-halo causes the largest shift in the exclusion limits and allowed regions set by different direct detection experiments in the plane of DM mass and scattering cross section compared to the SHM. Future data from space observatories such as Gaia can in principle set stringent constraints on the value of the local DM density, and such constraints could be used in future numerical simulations.

- The shift in the tail of the halo integral to higher minimum velocities compared to the SHM Maxwellian for some haloes results in a shift of a few GeV at low DM masses in the allowed regions and exclusion limits.

- The overall shift in all regions and exclusion limits due to the different local DM distribution of the MW-like haloes compared to the SHM, occurs in the same direction and compatibility between different experiments is not improved.

We have therefore shown that, when baryons are included in the EAGLE and APOSTLE high resolution hydrodynamic simulations in such a way that the main galaxy population properties are broadly reproduced, a Maxwellian velocity distribution with a most probable speed larger than the standard value assumed in the SHM describes well the local DM velocity distribution of simulated MW analogues. The local DM density obtained from the simulations is in agreement with global and local estimates.

Shortly after the submission of this work, the preprints by Kelso *et al.* [86] and Sloane *et al.* [87] appeared, studying the local DM distribution of MW-like galaxies in hydrodynamic simulations and the implications for direct detection. In general we agree with the conclusions of ref. [86], which studies two MW-like galaxies from the MaGICC cosmological simulations. They find that the SHM with velocity distribution inferred from the mass distribution of each simulated halo provides a reasonable fit in both of the MW-like galaxies they considered. Analogous to our findings, they also find that when baryons are included in the simulation, the best fit Maxwellian velocity distribution provides a good fit to the velocity distribution of each simulated halo. Ref. [87] considers four MW-like galaxies with different merger histories in high resolution simulations. Their results agree with ours and those of ref. [86] in finding that including baryons in the simulations leads to a shift of the DM speed distributions to larger speeds. However, our results differ in that ref. [87] finds a deficit of high speed DM particles in their simulations with baryons compared to the SHM (with a local circular speed

of 220 km/s). The halo integrals obtained from their best fit Maxwellian velocity distributions (with peak speeds smaller than 220 km/s), however, show only small discrepancies at high speeds compared to those obtained from the simulations. The difference between the best fit peak speeds of the Maxwellian distribution in our works is likely due to the different stellar masses of our MW-like galaxies, given the strong correlation between the stellar mass and local circular velocity as shown in figure 1.

We would like to stress again that the results of this work as well as refs. [86, 87] show that the halo integrals and hence direct detection event rates obtained from a Maxwellian velocity distribution with a free peak speed are similar to those obtained directly from the local DM velocity distributions of the simulated MW analogues. Thus a Maxwellian velocity distribution with a peak speed constrained by hydrodynamic simulations as well as observations could be used by the community when analysing the results of direct detection experiments.

Acknowledgements

---

[2] http://code.google.com/p/pyminuit

A Alternative selection of Milky Way analogues

In this appendix we present the velocity distributions and halo integrals for the two haloes in the EAGLE HR simulation that satisfy all three selection criteria discussed in section 3. These two haloes contain a substantial disc component, in addition to satisfying criteria (i) and (ii).

In figure 10, we show the local DM velocity modulus distribution in the Galactic rest frame for the two haloes (E9 and E11) satisfying criteria (i), (ii), and (iii) in the EAGLE HR hydrodynamic simulation (left panel) and DMO simulation (right panel). The SHM Maxwellian with peak speed of 230 km/s (solid black line), as well as the best fit Maxwellian distributions (dashed coloured lines) are also shown for comparison. The velocity distributions are not well fit by the SHM Maxwellian and are instead best fitted by the empirical fitting function of Mao *et al.* [33] (eq. (4.3)). The best fit parameters in eq. (4.3) are $v_0 = 250$ km/s and $p = 3.1$ with a reduced χ^2 of 1.6 for the best fit halo (E11), and $v_0 = 394$ km/s, and $p = 4.8$ with a reduced χ^2 of 2.6 for the other halo (E9). By comparing the two panels of figure 10, one observes that the peak of the distributions in the DMO simulation is shifted to smaller velocities compared to the hydrodynamic case.

Figure 11 shows the components of the DM velocity distribution for the same two haloes in the hydrodynamic (left panels) and DMO (right panels) simulations. The best fit Gaussian and generalized Gaussian distributions are also shown as solid and dashed coloured lines, respectively. The generalized Gaussian distribution gives the best fit to the radial and vertical components of the DM velocity distribution, while the double Gaussian gives a slightly better fit to the azimuthal velocity distribution (for a few haloes there is evidence for overfitting meaning that there is too much freedom in the fitting function). The two haloes do not have a significant non-zero mean azimuthal speed and hence there is no evidence for a dark disc component.

The average DM density in the torus located at the Solar position is $0.44 - 0.65$ GeV/cm^3 for the hydrodynamic case and $0.27 - 0.53$ GeV/cm^3 for the DMO case. While the average DM density in a shell centred at 8 kpc is $0.45 - 0.63$ GeV/cm^3 for the hydrodynamic case, comparable to the DM density in the torus.

In figure 12 we show the time-averaged halo integrals (Eq. 6.6) as a function $v_{\min}$ for the two haloes in the hydrodynamic (left panel) and DMO (right panel) simulations. The halo integrals computed from the mean value of the velocity distribution are shown by solid coloured lines, while the shaded bands are obtained by adding and subtracting 1σ to the mean velocity distribution. The halo integral for the SHM Maxwellian and the best fit Maxwellian are shown by solid black, and dashed coloured lines for each halo (with matching colours), respectively. One can see from the left panel that the dashed lines fall within the 1σ uncertainty band of the halo integrals for both haloes in the hydrodynamic simulation. In the DMO simulation however, the halo integrals deviate from the best fit Maxwellian at higher minimum velocities.

Finally, in figure 13, we use the DM distribution for the two haloes to analyse the data from direct detection experiments. The left panel of figure 13 shows the allowed regions from DAMA and CDMS-Si and exclusion limits from LUX and SuperCDMS in the DM mass and spin-independent cross section plane for the two haloes. In the right panel, we show the results for the same two haloes in the left panel but assuming the value of 0.3 GeV/cm^3 for the
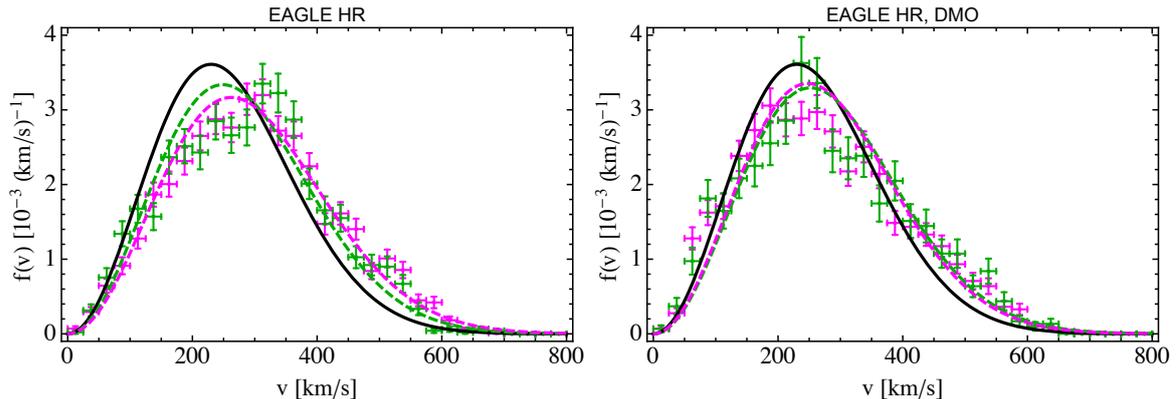
Figure 10.   Same as figure 2, but for the two haloes in the EAGLE HR simulation (E9 shown in green and E11 shown in magenta) which satisfy all three selection criteria discussed in section 3.

local DM density of both haloes. The conclusions remain the same as before. Namely, when fixing the local DM density to the value assumed in the SHM, the shift in the exclusion limits at large DM masses disappears. The high velocity tail of the DM distribution is responsible for the shift in the preferred regions and exclusion limits at low DM masses. While the general shift with respect to the SHM at all masses is due to the variation in the local DM density.

B   Dark matter velocity distribution

In figure 14 we show the DM velocity modulus distributions in the Galactic rest frame for the haloes in the EAGLE HR hydrodynamic simulation which satisfy our selection criteria (i) and (ii) and have the smallest (halo E6) and largest (halo E4) local DM density in our halo sample, 0.42 and 0.73 GeV/cm^3, respectively. The local DM densities in the torus for the same haloes in the DMO simulation are 0.49 and 0.46 GeV/cm^3, respectively. The left panel of figure 14 corresponds to the hydrodynamic case, while the right panel shows the results for the DMO case. The SHM Maxwellian (solid black line) and the best fit Maxwellians (dashed coloured lines) are also plotted for comparison.

C   Best fit parameters for velocity distributions

In tables 2 and 3 we quote the best fit parameters for three fitting functions, eq. (4.2) (with free parameter α, and $\alpha = 1$), eq. (4.3), and eq. (4.4), presented in section 4.1 to fit the DM velocity modulus distribution of the hydrodynamic and DMO haloes, respectively.

In tables 4 and 5 we present the best-fit parameters for the fit with Gaussian and generalized Gaussian functions to the radial and vertical velocity components for the selected MW-like haloes in the hydrodynamic simulations. In tables 6 and 7, we present the results of the fits with Gaussian, generalized Gaussian and double Gaussian functions for the azimuthal component of the DM velocity distribution. The results are discussed in section 4.2.

Figure 11. Same as figure 4, but for the two haloes in the EAGLE HR simulation which satisfy all three selection criteria discussed in section 3.

References

[1] R. Bernabei, P. Belli, F. Cappella, V. Caracciolo, S. Castellano, et al., *Final model independent result of DAMA/LIBRA-phase1*, *Eur.Phys.J.* **C73** (2013) 2648, [arXiv:1308.5109].

[2] **CDMS Collaboration** Collaboration, R. Agnese et al., *Silicon Detector Dark Matter Results from the Final Exposure of CDMS II*, *Phys.Rev.Lett.* **111** (2013) 251301, [arXiv:1304.4279].

[3] **LUX Collaboration** Collaboration, D. Akerib et al., *First results from the LUX dark matter experiment at the Sanford Underground Research Facility*, *Phys.Rev.Lett.* **112** (2014) 091303,
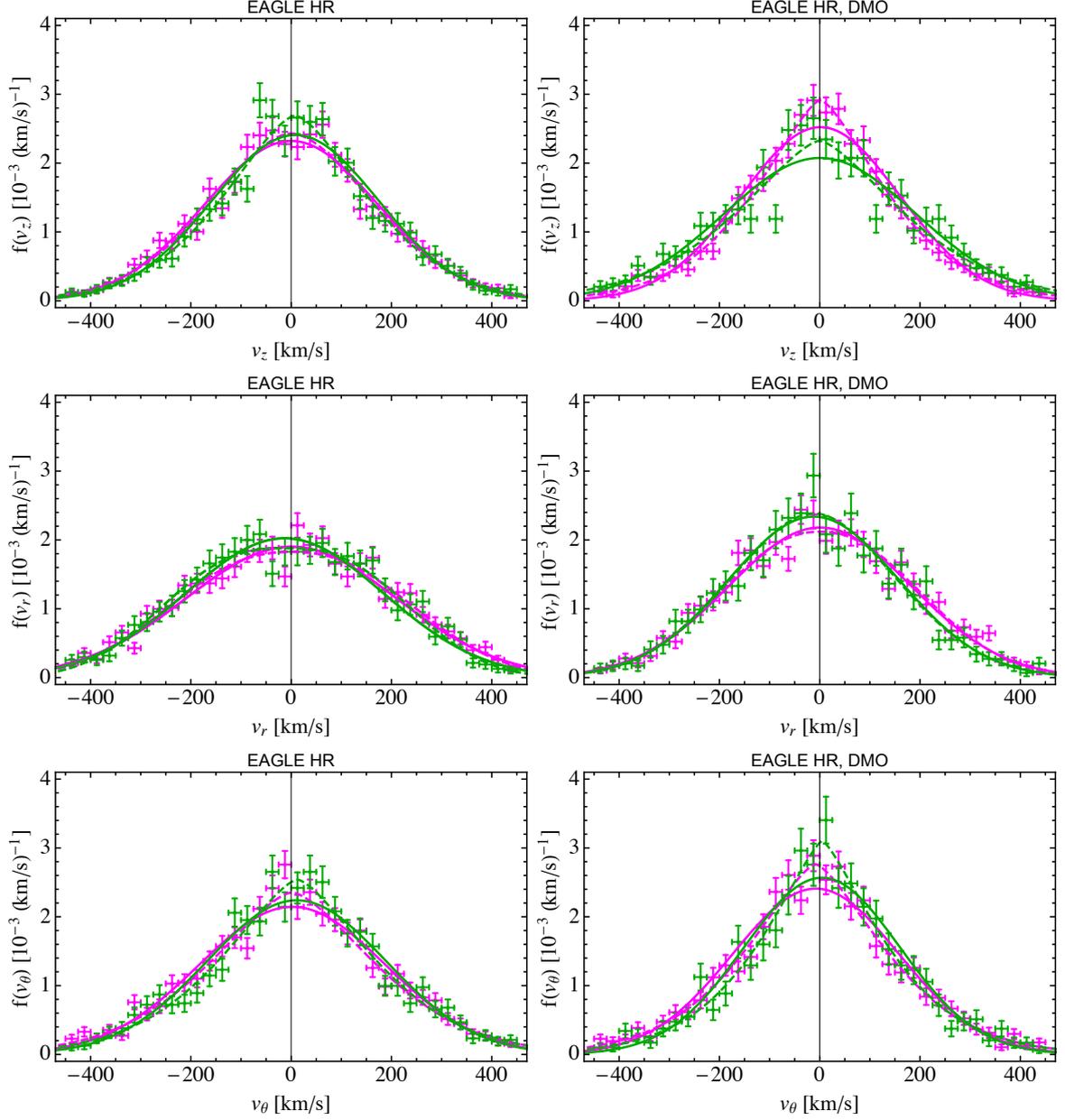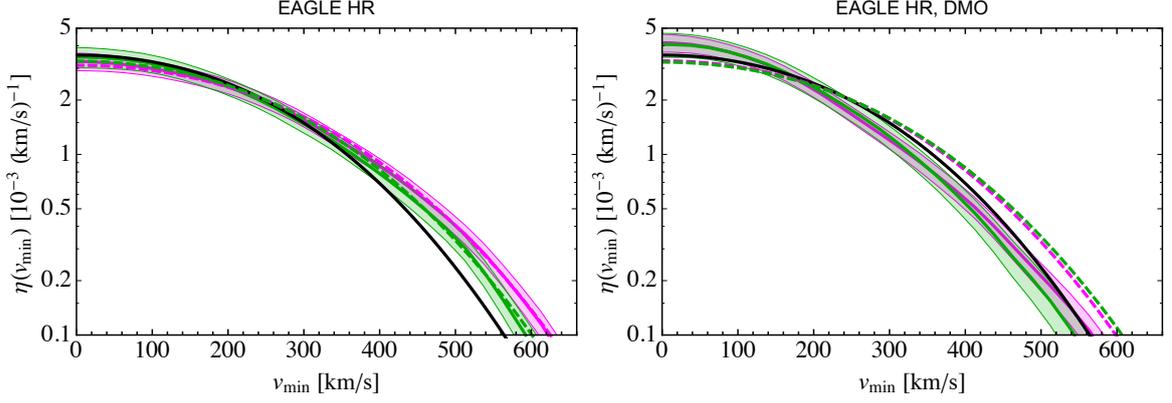
Figure 12. Same as figure 7, but for the two haloes in the EAGLE HR simulation which satisfy all three selection criteria discussed in section 3.
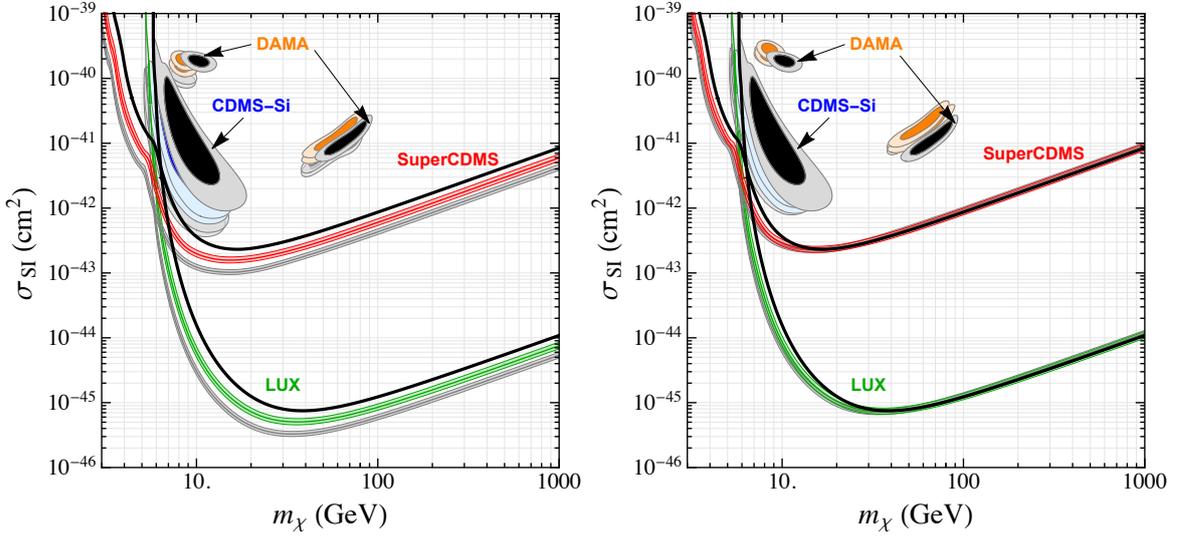
Figure 13. Same as figure 9 but for the two haloes in the EAGLE HR simulation which satisfy all three selection criteria.

[arXiv:1310.8214].

[4] **SuperCDMS Collaboration** Collaboration, R. Agnese et al., *Search for Low-Mass WIMPs with SuperCDMS, Phys.Rev.Lett.* **112** (2014) 241302, [arXiv:1402.7137].

[5] F. Iocco, M. Pato, and G. Bertone, *Evidence for dark matter in the inner Milky Way, Nature Phys.* **11** (2015) 245?248, [arXiv:1502.03821].

[6] P. J. Fox, J. Liu, and N. Weiner, *Integrating Out Astrophysical Uncertainties, Phys.Rev.* **D83** (2011) 103514, [arXiv:1011.1915].

[7] P. J. Fox, G. D. Kribs, and T. M. Tait, *Interpreting Dark Matter Direct Detection Independently of the Local Velocity and Density Distribution, Phys.Rev.* **D83** (2011) 034007, [arXiv:1011.1910].
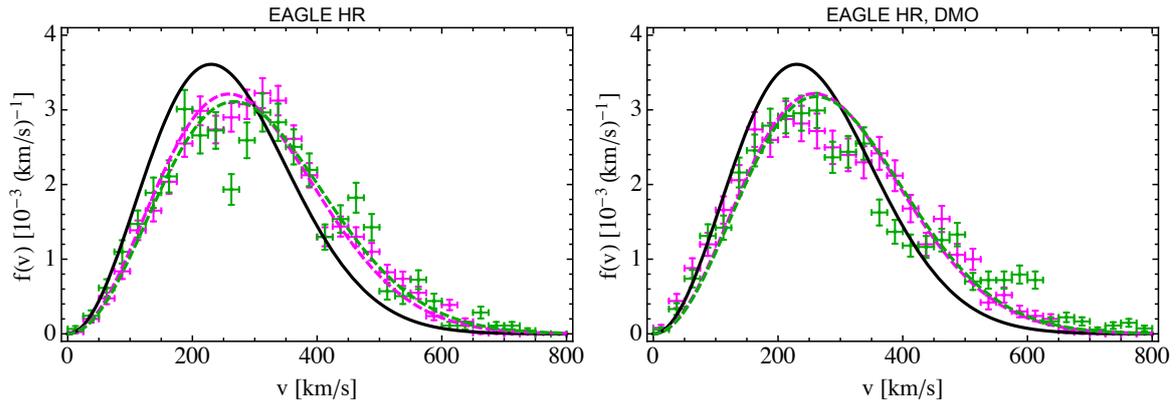
Figure 14. Same as figure 2, but for the two haloes in the EAGLE HR simulation with smallest (halo E6) and largest (halo E4) local DM density in the hydrodynamic case (left panel), and their DMO counterparts (right panel).

[8] C. McCabe, *DAMA and CoGeNT without astrophysical uncertainties*, *Phys.Rev.* **D84** (2011) 043525, [arXiv:1107.0741].

[9] M. T. Frandsen, F. Kahlhoefer, C. McCabe, S. Sarkar, and K. Schmidt-Hoberg, *Resolving astrophysical uncertainties in dark matter direct detection*, *JCAP* **1201** (2012) 024, [arXiv:1111.0292].

[10] P. Gondolo and G. B. Gelmini, *Halo independent comparison of direct dark matter detection data*, *JCAP* **1212** (2012) 015, [arXiv:1202.6359].

[11] J. Herrero-Garcia, T. Schwetz, and J. Zupan, *Astrophysics independent bounds on the annual modulation of dark matter signals*, *Phys.Rev.Lett.* **109** (2012) 141301, [arXiv:1205.0134].

[12] M. T. Frandsen, F. Kahlhoefer, C. McCabe, S. Sarkar, and K. Schmidt-Hoberg, *The unbearable lightness of being: CDMS versus XENON*, arXiv:1304.6066.

[13] E. Del Nobile, G. B. Gelmini, P. Gondolo, and J.-H. Huh, *Halo-independent analysis of direct detection data for light WIMPs*, arXiv:1304.6183.

[14] N. Bozorgnia, J. Herrero-Garcia, T. Schwetz, and J. Zupan, *Halo-independent methods for inelastic dark matter scattering*, arXiv:1305.3575.

[15] E. Del Nobile, G. Gelmini, P. Gondolo, and J.-H. Huh, *Generalized Halo Independent Comparison of Direct Dark Matter Detection Data*, *JCAP* **1310** (2013) 048, [arXiv:1306.5273].

[16] E. Del Nobile, G. B. Gelmini, P. Gondolo, and J.-H. Huh, *Update on Light WIMP Limits: LUX, lite and Light*, *JCAP* **1403** (2014) 014, [arXiv:1311.4247].

[17] B. Feldstein and F. Kahlhoefer, *A new halo-independent approach to dark matter direct detection analysis*, *JCAP* **1408** (2014) 065, [arXiv:1403.4606].

[18] P. J. Fox, Y. Kahn, and M. McCullough, *Taking Halo-Independent Dark Matter Methods Out of the Bin*, *JCAP* **1410** (2014), no. 10 076, [arXiv:1403.6830].

[19] J. F. Cherry, M. T. Frandsen, and I. M. Shoemaker, *Halo Independent Direct Detection of Momentum-Dependent Dark Matter*, *JCAP* **1410** (2014), no. 10 022, [arXiv:1405.1420].

[20] B. Feldstein and F. Kahlhoefer, *Quantifying (dis)agreement between direct detection*

experiments in a halo-independent way, JCAP **1412** (2014), no. 12 052, [arXiv:1409.5446].

[21] N. Bozorgnia and T. Schwetz, *What is the probability that direct detection experiments have observed Dark Matter?*, JCAP **1412** (2014), no. 12 015, [arXiv:1410.6160].

[22] A. J. Anderson, P. J. Fox, Y. Kahn, and M. McCullough, *Halo-Independent Direct Detection Analyses Without Mass Assumptions*, JCAP **1510** (2015), no. 10 012, [arXiv:1504.03333].

[23] M. Blennow, J. Herrero-Garcia, T. Schwetz, and S. Vogl, *Halo-independent tests of dark matter direct detection signals: local DM density, LHC, and thermal freeze-out*, JCAP **1508** (2015), no. 08 039, [arXiv:1505.05710].

[24] F. Ferrer, A. Ibarra, and S. Wild, *A novel approach to derive halo-independent limits on dark matter properties*, JCAP **1509** (2015), no. 09 052, [arXiv:1506.03386].

[25] G. B. Gelmini, A. Georgescu, P. Gondolo, and J.-H. Huh, *Extended Maximum Likelihood Halo-independent Analysis of Dark Matter Direct Detection Data*, arXiv:1507.03902.

[26] M. Vogelsberger, A. Helmi, V. Springel, S. D. M. White, J. Wang, C. S. Frenk, A. Jenkins, A. D. Ludlow, and J. F. Navarro, *Phase-space structure in the local dark matter distribution and its signature in direct detection experiments*, Mon. Not. Roy. Astron. Soc. **395** (2009) 797–811, [arXiv:0812.0362].

[27] M. Kuhlen, N. Weiner, J. Diemand, P. Madau, B. Moore, D. Potter, J. Stadel, and M. Zemp, *Dark Matter Direct Detection with Non-Maxwellian Velocity Structure*, JCAP **1002** (2010) 030, [arXiv:0912.2358].

[28] C. W. Purcell, A. R. Zentner, and M.-Y. Wang, *Dark Matter Direct Search Rates in Simulations of the Milky Way and Sagittarius Stream*, JCAP **1208** (2012) 027, [arXiv:1203.6617].

[29] F. S. Ling, E. Nezri, E. Athanassoula, and R. Teyssier, *Dark Matter Direct Detection Signals inferred from a Cosmological N-body Simulation with Baryons*, JCAP **1002** (2010) 012, [arXiv:0909.2028].

[30] C. Tsallis, *Possible Generalization of Boltzmann-Gibbs Statistics*, J. Statist. Phys. **52** (1988) 479–487.

[31] L. Beraldo e Silva, G. A. Mamon, M. Duarte, R. Wojtak, S. Peirani, and G. Bou, *Anisotropic q-Gaussian 3D velocity distributions in ?CDM haloes*, Mon. Not. Roy. Astron. Soc. **452** (2015), no. 1 944–955, [arXiv:1310.6756].

[32] M. Kuhlen, A. Pillepich, J. Guedes, and P. Madau, *The Distribution of Dark Matter in the Milky Way's Disk*, Astrophys. J. **784** (2014) 161, [arXiv:1308.1703].

[33] Y.-Y. Mao, L. E. Strigari, R. H. Wechsler, H.-Y. Wu, and O. Hahn, *Halo-to-Halo Similarity and Scatter in the Velocity Distribution of Dark Matter*, Astrophys. J. **764** (2013) 35, [arXiv:1210.2721].

[34] I. Butsky, A. V. Macci, A. A. Dutton, L. Wang, G. S. Stinson, C. Penzo, X. Kang, B. W. Keller, and J. Wadsley, *NIHAO project II: Halo shape, phase-space density and velocity distribution of dark matter in galaxy formation simulations*, arXiv:1503.04814.

[35] J. Schaye, R. A. Crain, R. G. Bower, M. Furlong, M. Schaller, T. Theuns, C. Dalla Vecchia, C. S. Frenk, I. G. McCarthy, J. C. Helly, A. Jenkins, Y. M. Rosas-Guevara, S. D. M. White, M. Baes, C. M. Booth, P. Camps, J. F. Navarro, Y. Qu, A. Rahmati, T. Sawala, P. A. Thomas, and J. Trayford, *The EAGLE project: simulating the evolution and assembly of galaxies and their environments*, MNRAS **446** (Jan., 2015) 521–554, [arXiv:1407.7040].

[36] R. A. Crain, J. Schaye, R. G. Bower, M. Furlong, M. Schaller, T. Theuns, C. Dalla Vecchia,

C. S. Frenk, I. G. McCarthy, J. C. Helly, A. Jenkins, Y. M. Rosas-Guevara, S. D. M. White, and J. W. Trayford, *The EAGLE simulations of galaxy formation: calibration of subgrid physics and model variations*, MNRAS **450** (June, 2015) 1937–1961, [`arXiv:1501.01311`].

[37] T. Sawala, C. S. Frenk, A. Fattahi, J. F. Navarro, R. G. Bower, R. A. Crain, C. Dalla Vecchia, M. Furlong, J. C. Helly, A. Jenkins, K. A. Oman, M. Schaller, J. Schaye, T. Theuns, J. Trayford, and S. D. M. White, *The APOSTLE simulations: solutions to the Local Group's cosmic puzzles*, ArXiv e-prints (Nov., 2015) [`arXiv:1511.01098`].

[38] A. Fattahi, J. F. Navarro, T. Sawala, C. S. Frenk, K. A. Oman, R. A. Crain, M. Furlong, M. Schaller, J. Schaye, T. Theuns, and A. Jenkins, *The APOSTLE project: Local Group kinematic mass constraints and simulation candidate selection*, ArXiv e-prints (July, 2015) [`arXiv:1507.03643`].

[39] F. Calore, N. Bozorgnia, M. Lovell, G. Bertone, M. Schaller, C. S. Frenk, R. A. Crain, J. Schaye, T. Theuns, and J. W. Trayford, *Simulated Milky Way analogues: implications for dark matter indirect searches*, J. Cosmology Astropart. Phys. **12** (Dec., 2015) 053, [`arXiv:1509.02164`].

[40] C. Dalla Vecchia et al., *Anarchy-SPH: state of the art smoothed particle hydrodynamics and entropy mixing*, in prep.

[41] M. Schaller, C. Dalla Vecchia, J. Schaye, R. G. Bower, T. Theuns, R. A. Crain, M. Furlong, and I. G. McCarthy, *The EAGLE simulations of galaxy formation: the importance of the hydrodynamics scheme*, MNRAS **454** (Dec., 2015) 2277–2291, [`arXiv:1509.05056`].

[42] V. Springel, *The cosmological simulation code GADGET-2*, MNRAS **364** (Dec., 2005) 1105–1134, [`astro-ph/0505010`].

[43] R. P. C. Wiersma, J. Schaye, and B. D. Smith, *The effect of photo-ionization on the cooling rates of enriched, astrophysical plasmas*, Mon. Not. Roy. Astron. Soc. **393** (2009) 99–107, [`arXiv:0807.3748`].

[44] R. P. C. Wiersma, J. Schaye, T. Theuns, C. Dalla Vecchia, and L. Tornatore, *Chemical enrichment in cosmological, smoothed particle hydrodynamics simulations*, Mon. Not. Roy. Astron. Soc. **399** (2009) 574–600, [`arXiv:0902.1535`].

[45] J. Schaye and C. Dalla Vecchia, *On the relation between the Schmidt and Kennicutt-Schmidt star formation laws and its implications for numerical simulations*, Mon. Not. Roy. Astron. Soc. **383** (2008) 1210, [`arXiv:0709.0292`].

[46] C. D. Vecchia and J. Schaye, *Simulating galactic outflows with thermal supernova feedback*, Mon. Not. Roy. Astron. Soc. **426** (2012) 140, [`arXiv:1203.5667`].

[47] Y. M. Rosas-Guevara, R. G. Bower, J. Schaye, M. Furlong, C. S. Frenk, C. M. Booth, R. Crain, C. D. Vecchia, M. Schaller, and T. Theuns, *The impact of angular momentum on black hole accretion rates in simulations of galaxy formation*, Mon. Not. Roy. Astron. Soc. **454** (2015), no. 1 1038–1057, [`arXiv:1312.0598`].

[48] Planck Collaboration, P. A. R. Ade, N. Aghanim, C. Armitage-Caplan, M. Arnaud, M. Ashdown, F. Atrio-Barandela, J. Aumont, C. Baccigalupi, A. J. Banday, and et al., *Planck 2013 results. XVI. Cosmological parameters*, A&A **571** (Nov., 2014) A16, [`arXiv:1303.5076`].

[49] P. J. McMillan, *Mass models of the Milky Way*, Mon.Not.Roy.Astron.Soc. **414** (2011) 2446–2457, [`arXiv:1102.4340`].

[50] R. Schönrich, J. Binney, and W. Dehnen, *Local kinematics and the local standard of rest*, MNRAS **403** (Apr., 2010) 1829–1833, [`arXiv:0912.3693`].

[51] M. T. Busha, P. J. Marshall, R. H. Wechsler, A. Klypin, and J. Primack, *The Mass*

Distribution and Assembly of the Milky Way from the Properties of the Magellanic Clouds, *Astrophys.J.* **743** (2011) 40, [arXiv:1011.2203].

[52] M. Lisanti, L. E. Strigari, J. G. Wacker, and R. H. Wechsler, *The Dark Matter at the End of the Galaxy*, *Phys.Rev.* **D83** (2011) 023519, [arXiv:1010.4300].

[53] T. Piffl et al., *The RAVE survey: the Galactic escape speed and the mass of the Milky Way*, *Astron. Astrophys.* **562** (2014) A91, [arXiv:1309.4293].

[54] J. I. Read, G. Lake, O. Agertz, and V. P. Debattista, *Thin, thick and dark discs in LCDM*, *Mon. Not. Roy. Astron. Soc.* **389** (2008) 1041–1057, [arXiv:0803.2714].

[55] J. I. Read, L. Mayer, A. M. Brooks, F. Governato, and G. Lake, *A dark matter disc in three cosmological simulations of Milky Way mass galaxies*, *Mon. Not. Roy. Astron. Soc.* **397** (2009) 44, [arXiv:0902.0009].

[56] C. W. Purcell, J. S. Bullock, and M. Kaplinghat, *The Dark Disk of the Milky Way*, *Astrophys. J.* **703** (2009) 2275–2284, [arXiv:0906.5348].

[57] T. Bruch, J. Read, L. Baudis, and G. Lake, *Detecting the Milky Way's Dark Disk*, *Astrophys. J.* **696** (2009) 920–923, [arXiv:0804.2896].

[58] D. G. Algorry, J. F. Navarro, M. G. Abadi, L. V. Sales, M. Steinmetz, and F. Piontek, *Counterrotating stars in simulated galaxy discs*, *Mon. Not. Roy. Astron. Soc.* **437** (2014), no. 4 3596–3602, [arXiv:1311.1215].

[59] R. Catena and P. Ullio, *A novel determination of the local dark matter density*, *JCAP* **1008** (2010) 004, [arXiv:0907.0018].

[60] M. Weber and W. de Boer, *Determination of the Local Dark Matter Density in our Galaxy*, *Astron. Astrophys.* **509** (2010) A25, [arXiv:0910.4272].

[61] F. Iocco, M. Pato, G. Bertone, and P. Jetzer, *Dark Matter distribution in the Milky Way: microlensing and dynamical constraints*, *JCAP* **1111** (2011) 029, [arXiv:1107.5810].

[62] F. Nesti and P. Salucci, *The Dark Matter halo of the Milky Way, AD 2013*, *JCAP* **1307** (2013) 016, [arXiv:1304.5127].

[63] Y. Sofue, *Dark halos of M?31 and the Milky Way*, *Publ. Astron. Soc. Jap.* **67** (2015), no. 4 75, [arXiv:1504.05368].

[64] M. Pato, F. Iocco, and G. Bertone, *Dynamical constraints on the dark matter distribution in the Milky Way*, *JCAP* **1512** (2015), no. 12 001, [arXiv:1504.06324].

[65] P. Salucci, F. Nesti, G. Gentile, and C. F. Martins, *The dark matter density at the Sun's location*, *Astron. Astrophys.* **523** (2010) A83, [arXiv:1003.3101].

[66] M. C. Smith, S. H. Whiteoak, and N. W. Evans, *Slicing and dicing the Milky Way disk in SDSS*, *Astrophys. J.* **746** (2012) 181, [arXiv:1111.6920].

[67] J. Bovy and S. Tremaine, *On the local dark matter density*, *Astrophys. J.* **756** (2012) 89, [arXiv:1205.4033].

[68] S. Garbari, C. Liu, J. I. Read, and G. Lake, *A new determination of the local dark matter density from the kinematics of K dwarfs*, *Mon. Not. Roy. Astron. Soc.* **425** (2012) 1445, [arXiv:1206.0015].

[69] L. Zhang, H.-W. Rix, G. van de Ven, J. Bovy, C. Liu, and G. Zhao, *The Gravitational Potential Near the Sun From SEGUE K-dwarf Kinematics*, *Astrophys. J.* **772** (2013) 108, [arXiv:1209.0256].

[70] J. Bovy and H.-W. Rix, *A Direct Dynamical Measurement of the Milky Way's Disk Surface*

Density Profile, Disk Scale Length, and Dark Matter Profile at 4 kpc $\lesssim R \lesssim$ 9 kpc, Astrophys. J. **779** (2013) 115, [arXiv:1309.0809].

[71] M. Schaller, C. S. Frenk, R. G. Bower, T. Theuns, A. Jenkins, J. Schaye, R. A. Crain, M. Furlong, C. Dalla Vecchia, and I. G. McCarthy, *Baryon effects on the internal structure of ΛCDM haloes in the EAGLE simulations*, MNRAS **451** (Aug., 2015) 1247–1267, [arXiv:1409.8617].

[72] J. Dubinski, *The effect of dissipation on the shapes of dark halos*, ApJ **431** (Aug., 1994) 617–624, [astro-ph/9309001].

[73] S. E. Bryan, S. T. Kay, A. R. Duffy, J. Schaye, C. Dalla Vecchia, and C. M. Booth, *The impact of baryons on the spins and shapes of dark matter haloes*, MNRAS **429** (Mar., 2013) 3316–3329, [arXiv:1207.4555].

[74] M. Schaller, C. S. Frenk, T. Theuns, F. Calore, G. Bertone, N. Bozorgnia, R. A. Crain, A. Fattahi, J. F. Navarro, T. Sawala, and J. Schaye, *Dark matter annihilation radiation in hydrodynamic simulations of Milky Way haloes*, MNRAS **455** (Feb., 2016) 4442–4451, [arXiv:1509.02166].

[75] R. H. Helm, *Inelastic and Elastic Scattering of 187-Mev Electrons from Selected Even-Even Nuclei*, Phys.Rev. **104** (1956) 1466–1475.

[76] R. Schoenrich, J. Binney, and W. Dehnen, *Local Kinematics and the Local Standard of Rest*, Mon.Not.Roy.Astron.Soc. **403** (2010) 1829, [arXiv:0912.3693].

[77] G. Gelmini and P. Gondolo, *WIMP annual modulation with opposite phase in Late-Infall halo models*, Phys.Rev. **D64** (2001) 023504, [hep-ph/0012315].

[78] A. M. Green, *Effect of realistic astrophysical inputs on the phase and shape of the WIMP annual modulation signal*, Phys. Rev. **D68** (2003) 023004, [astro-ph/0304446].

[79] R. Bernabei, P. Belli, V. Landoni, F. Montecchia, W. Di Nicolantonio, et al., *New limits on WIMP search with large-mass low-radioactivity NaI(Tl) set-up at Gran Sasso*, Phys.Lett. **B389** (1996) 757–766.

[80] M. Fairbairn and T. Schwetz, *Spin-independent elastic WIMP scattering and the DAMA annual modulation signal*, JCAP **0901** (2009) 037, [arXiv:0808.0704].

[81] J. Kopp, T. Schwetz, and J. Zupan, *Global interpretation of direct Dark Matter searches after CDMS-II results*, JCAP **1002** (2010) 014, [arXiv:0912.4264].

[82] J. Kopp, T. Schwetz, and J. Zupan, *Light Dark Matter in the light of CRESST-II*, JCAP **1203** (2012) 001, [arXiv:1110.2721].

[83] N. Bozorgnia, R. Catena, and T. Schwetz, *Anisotropic dark matter distribution functions and impact on WIMP direct detection*, JCAP **1312** (2013) 050, [arXiv:1310.0468].

[84] K. A. McCarthy, "Dark matter search results from the silicon detectors of the cryogenic dark matter search experiment." Presented at the APS Physics Meeting, Denver, Colorado, 2013.

[85] S. Yellin, *Finding an upper limit in the presence of unknown background*, Phys. Rev. **D66** (2002) 032005, [physics/0203002].

[86] C. Kelso, C. Savage, M. Valluri, K. Freese, G. S. Stinson, and J. Bailin, *The impact of baryons on the direct detection of dark matter*, arXiv:1601.04725.

[87] J. D. Sloane, M. R. Buckley, A. M. Brooks, and F. Governato, *Assessing Astrophysical Uncertainties in Direct Detection with Galaxy Simulations*, arXiv:1601.05402.

Halo Name	Maxwellian		Generalized Maxw.			Mao *et al.*			Lisanti *et al.*		
	v_0 [km/s]	$\tilde{\chi}^2$	v_0 [km/s]	α	$\tilde{\chi}^2$	v_0 [km/s]	p	$\tilde{\chi}^2$	v_0 [km/s]	k	$\tilde{\chi}^2$
E1	287.73	3.77	189.56	0.68	1.05	154.48	3.18	1.03	287.73	0.03	3.90
E2	266.01	2.68	227.12	0.85	2.14	206.14	4.98	2.00	266.01	0.02	2.77
E3	288.64	1.47	294.02	1.02	1.51	267.35	3.76	0.82	296.49	1.86	1.26
E4	258.53	3.81	284.30	1.12	3.35	317.74	4.21	2.51	282.08	2.65	2.70
E5	249.99	4.39	277.30	1.13	4.10	408.10	5.79	2.81	321.47	4.80	3.39
E6	266.97	3.52	227.81	0.85	3.24	198.93	3.54	2.98	266.97	0.02	3.65
E7	270.84	3.67	254.67	0.93	3.68	240.96	3.69	3.87	270.96	0.77	3.81
E8	258.23	2.86	217.95	0.84	2.10	166.91	2.69	1.61	258.30	0.63	2.97
E9	248.81	4.19	288.70	1.20	3.73	393.63	4.82	2.58	342.49	4.36	3.05
E10	261.78	2.49	274.11	1.06	2.51	281.33	3.41	1.17	282.77	2.21	1.92
E11	262.27	2.77	279.94	1.08	2.67	250.06	3.14	1.57	276.42	1.87	2.10
E12	231.90	1.43	252.25	1.11	0.99	467.84	5.69	1.53	245.72	2.67	1.02
A1	222.93	3.74	212.25	0.95	3.73	186.32	3.29	2.02	224.89	0.54	3.40
A2	234.35	10.35	213.58	0.91	10.50	136.41	1.07	3.52	243.23	0.64	8.25

Table 2. Best-fit parameters for the velocity modulus distribution of the selected galaxies in the EAGLE HR (E1 to E12) and APOSTLE IR (A1 and A2) simulations, adopting the three different fitting functions explained in the main text (eqs. (4.2), (4.3), (4.4)) and, additionally, a standard Maxwellian distribution (α fixed to 1 in eq. (4.2)). Besides the best-fit parameters, we quote the reduced χ^2, $\tilde{\chi}^2 \equiv \chi^2/(N - dof)$, where $dof = 2$ for the three fitting functions and $dof = 1$ for the standard Maxwellian.

Halo Name	Maxwellian		Generalized Maxw.			Mao *et al.*			Lisanti *et al.*		
	v_0 [km/s]	$\tilde{\chi}^2$	v_0 [km/s]	α	$\tilde{\chi}^2$	v_0 [km/s]	p	$\tilde{\chi}^2$	v_0 [km/s]	k	$\tilde{\chi}^2$
E1 DMO	256.70	10.01	111.77	0.53	1.67	102.54	0.72	1.71	256.70	0.10	10.34
E2 DMO	225.25	4.51	130.74	0.63	1.39	108.62	3.27	1.23	225.25	0.82	4.66
E3 DMO	269.90	4.70	136.30	0.58	1.03	118.62	1.09	0.89	269.89	0.07	4.87
E4 DMO	258.08	2.95	214.39	0.83	2.37	163.45	2.58	1.13	259.07	1.06	3.04
E5 DMO	255.68	2.64	257.69	1.01	2.75	317.89	5.21	2.08	286.05	3.68	2.59
E6 DMO	261.30	6.02	161.41	0.65	2.31	123.45	1.20	2.47	261.27	0.02	6.22
E7 DMO	242.97	8.95	137.28	0.62	3.26	110.09	1.43	2.50	242.96	0.02	9.27
E8 DMO	252.84	6.54	139.17	0.61	1.52	112.50	0.91	1.45	252.81	0.02	6.77
E9 DMO	252.01	2.21	192.51	0.77	1.57	152.16	2.35	1.16	251.99	0.02	2.31
E10 DMO	258.78	5.06	182.65	0.74	3.99	147.44	2.00	2.83	258.72	0.01	5.26
E11 DMO	247.62	3.98	183.95	0.76	2.20	139.50	2.08	1.23	247.60	0.02	4.15
E12 DMO	229.90	1.61	200.62	0.87	1.33	163.08	3.35	0.65	230.09	0.90	1.68
A1 DMO	193.01	7.12	135.37	0.72	3.12	98.90	1.23	1.42	192.94	0.51	7.18
A2 DMO	221.86	3.50	168.10	0.77	2.16	116.88	1.12	0.94	221.78	0.66	3.57

Table 3. Same as table 2 for the corresponding DMO simulations.

Halo Name	Gaussian				Generalized Gaussian				
	v_0 [km/s]	μ [km/s]	σ_μ [km/s]	χ^2	v_0 [km/s]	μ [km/s]	σ_μ [km/s]	α	χ^2
E1	291.24	1.60	4.66	1.41	280.09	2.02	4.81	0.88	1.38
E2	282.12	-5.32	4.47	1.15	288.89	-5.39	4.39	1.08	1.15
E3	319.49	1.89	5.02	1.58	340.66	2.13	4.57	1.35	1.31
E4	304.65	5.39	4.44	1.91	328.51	4.51	3.93	1.44	1.39
E5	295.21	-6.11	4.57	0.83	307.12	-5.96	4.36	1.17	0.73
E6	282.13	-7.24	5.21	0.96	289.14	-7.11	5.10	1.09	0.97
E7	276.18	6.20	4.51	1.14	287.58	6.27	4.35	1.14	1.09
E8	274.78	1.23	4.35	1.44	293.53	-1.08	4.14	1.26	1.15
E9	278.69	-13.06	4.99	1.15	299.24	-10.96	4.59	1.32	0.83
E10	298.25	12.26	4.89	0.87	312.75	12.11	4.56	1.23	0.71
E11	296.73	0.24	4.48	1.50	308.95	0.32	4.26	1.18	1.41
E12	235.80	1.76	3.09	1.44	257.97	1.25	2.98	1.26	0.83
A1	235.69	-1.35	2.49	1.29	243.91	-0.88	2.48	1.08	1.22
A2	273.70	-1.21	3.52	1.07	286.41	-1.08	3.41	1.15	0.95

Table 4. Best-fit parameters for the distribution of the radial velocity component, v_r, of the selected galaxies in the EAGLE HR (haloes E1 to E12) and APOSTLE IR (haloes A1 and A2) hydrodynamic simulations, adopting a Gaussian and a generalized Gaussian function. Besides the best-fit parameters, we quote the reduced χ^2, $\tilde{\chi}^2 \equiv \chi^2/(N - dof)$, where $dof = 2$ for the Gaussian function and $dof = 3$ for the generalized Gaussian.

Halo Name	Gaussian				Generalized Gaussian				
	v_0 [km/s]	μ [km/s]	σ_μ [km/s]	χ^2	v_0 [km/s]	μ [km/s]	σ_μ [km/s]	α	χ^2
E1	262.08	-1.52	3.98	1.03	243.43	-1.02	4.11	0.83	0.84
E2	237.27	-2.98	3.50	1.41	198.65	-2.74	3.60	0.70	0.54
E3	261.94	-4.63	3.66	1.96	220.15	-5.47	3.81	0.69	0.96
E4	219.83	1.13	2.81	0.92	205.46	1.82	2.86	0.87	0.69
E5	236.11	0.57	3.31	1.66	204.89	-0.38	3.39	0.75	1.00
E6	259.93	5.05	4.63	0.90	243.11	4.08	4.78	0.85	0.80
E7	283.42	-11.74	4.69	1.62	245.79	-11.82	4.97	0.71	1.07
E8	239.72	0.39	3.57	0.71	229.54	0.59	3.64	0.90	0.64
E9	234.25	8.29	3.89	1.23	206.72	8.08	3.98	0.77	0.85
E10	237.75	0.05	3.53	0.78	228.90	-0.06	3.57	0.92	0.75
E11	243.00	0.13	3.35	1.12	231.29	0.22	3.40	0.89	1.04
E12	197.79	2.68	2.52	1.91	173.20	2.94	2.54	0.77	1.14
A1	210.32	-3.68	2.17	1.88	186.41	-3.31	2.21	0.79	0.81
A2	222.02	4.87	2.64	2.68	183.71	6.04	2.64	0.72	1.21

Table 5. Same as table 4 for the distribution of the vertical velocity component, v_z.

Halo Name	Gaussian				Generalized Gaussian				
	v_0[km/s]	μ[km/s]	σ_μ[km/s]	χ^2	v_0[km/s]	μ[km/s]	σ_μ[km/s]	α	χ^2
E1	277.18	2.82	4.31	1.30	250.03	1.31	4.52	0.77	0.96
E2	257.62	-4.63	3.94	1.39	244.29	-3.11	4.12	0.88	1.33
E3	276.68	7.02	3.98	1.18	259.37	6.55	4.10	0.84	1.05
E4	265.46	-20.43	3.59	1.21	266.29	-20.44	3.58	1.01	1.25
E5	247.12	8.42	3.52	1.46	219.77	6.90	3.62	0.78	1.08
E6	247.07	3.50	4.30	1.22	215.85	3.74	4.36	0.76	0.88
E7	241.74	39.93	3.86	2.09	222.41	41.61	4.03	0.81	1.84
E8	235.53	13.86	3.47	2.55	180.26	12.03	3.43	0.61	0.88
E9	251.95	10.92	4.27	1.70	217.46	12.36	4.59	0.73	1.19
E10	266.72	23.90	4.13	1.39	248.16	24.18	4.31	0.82	1.20
E11	263.07	2.29	3.74	1.67	236.30	1.72	3.87	0.78	1.31
E12	230.57	64.55	3.13	2.63	218.91	66.16	3.28	0.87	2.54
A1	207.47	38.15	2.19	2.67	186.13	37.84	2.22	0.81	1.82
A2	212.30	-3.95	2.55	3.09	182.27	-0.88	2.61	0.75	2.02

Table 6. Same as table 4 for the distribution of the azimuthal velocity component, v_θ.

Halo Name	c_1	v_1 [km/s]	μ_1 [km/s]	σ_{μ_1} [km/s]	c_2	v_2 [km/s]	μ_2 [km/s]	σ_{μ_2} [km/s]	$\chi^2_{\mathrm{double\,Gauss}}$
E1	0.13	111.28	-21.95	14.40	0.87	303.24	6.99	5.99	0.87
E2	0.88	275.08	-14.91	6.77	0.12	112.76	54.91	15.24	1.01
E3	0.95	287.09	7.63	4.41	0.05	62.73	-6.72	13.79	0.90
E4	0.99	262.54	-21.85	3.58	0.01	13.20	420.94	2.95	1.08
E5	0.09	71.29	-10.48	9.70	0.91	261.96	11.39	4.25	0.85
E6	0.09	70.39	-4.38	11.62	0.91	262.29	5.23	5.11	0.81
E7	0.57	295.43	-10.19	22.52	0.43	165.06	88.48	12.74	0.87
E8	0.63	311.89	8.13	8.25	0.37	132.95	17.15	6.56	0.97
E9	0.81	284.78	9.11	6.46	0.19	116.02	17.27	11.53	1.14
E10	0.30	177.56	12.35	17.25	0.70	316.24	30.77	10.29	1.24
E11	0.92	277.68	1.79	4.68	0.08	76.26	2.45	20.46	1.32
E12	0.68	254.78	26.62	15.07	0.32	139.89	135.57	11.56	0.88
A1	0.53	252.62	7.61	10.75	0.47	153.16	63.98	5.84	1.00
A2	0.74	242.65	-16.23	4.62	0.26	112.55	28.11	6.90	1.44

Table 7. Best-fit parameters for the distribution of the azimuthal velocity component, v_θ, of the selected galaxies in the EAGLE HR (E1 to E12) and APOSTLE IR (A1 and A2) hydrodynamic simulations, adopting a double Gaussian, see text for more details.